Can energy directly be harvested from permanent magnets?

Lukas Kurmann[1],*

aABBTS, Höhere Fachschule für Technik und Informatik, Wiesenstrasse 26, Baden, 5400, Switzerland

Abstract
With regards to classical Electromagnetic (EM) Theory, a purely analytical approach with verification and validation is followed for describing and measuring asymmetric incommensurable torque (AIT) signals arising out of magnetic attraction and repulsion using moving 2D and 3D current loop structures. Validation is done statically, by comparing the nonlinear analytical EM spring with its measured counterpart and dynamically by showing an angular path and velocity difference of more than 1rad and 8rad/s by flipping the EM spring from its unstable position in clockwise and counterclockwise direction. Where the energy comes from, cannot yet be determined and only a hypothesis about the energy source can be given.
Keywords: *Lorentz Force; Permanent Magnet (PM); Analytical Approach; Parameter Model; Validation Experiments*

I.   Introduction

Permanent magnets are often modeled with current loops using methods like Biot- Savart [1] or Lorentz Force [2] approach and others [3]. The idea of using current loops for modeling PM is a common practice [4] for describing analytically magnetic fields to avoid a computational intensive FE approach. The analytical approach is also often used in lumped parameter models of kinetic energy harvesters (KEH), [5–7]. A new kind of KEH device that allegedly transfers magnetic field- in mechanical-energy has been patented in Europe in 2008 [8] and a modeling attempt was made in [9].
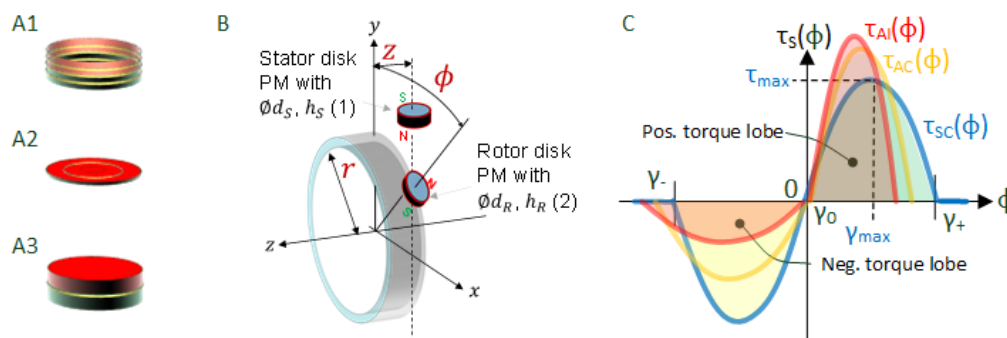

Fig. 1. PM modeling by means of current loops (shown in yellow, A1-3, lhs). Revolving rotor with disk PM's (in the middle, B). On rhs, C, generated torque signals due to nonlin. EM springs

In this manuscript, such devices are called magnetic energy harvesting (MEH) systems, as the primary source is magnetic energy, not kinetic energy (in contrast to the used nomenclature of [9]). Fig. 1 shows major components in this manuscript. In the section A different exemplarily PMs are shown (A1 shows a cylindrical shell PM, A2 a flat disk PM and A3 a cylinder PM). These PMs are modeled with direct current (DC) loops, see also following chapter II. In the middle, the setup is shown on which the created **B**-field from the stator PM (or the current loops, e.g., coil) will create forces on the rotor coil.

---

[1] Corresponding author.
Email address: lukas.kurmann@gmail.com (Dr.-Ing. Lukas Kurmann)

These forces create a torque signal $\tau_S(\phi)$ using shown degree of freedoms (DoF's) ϕ, r and z (Fig. 1, B). Three such generated torque signals (Fig. 1, C) are named symmetric commensurable-torque $\tau_{SC}(\phi)$ (shown in blue), asymmetric commensurable-torque $\tau_{AC}(\phi)$ (depicted in orange) and asymmetric incommensurable-torque $\tau_{AI}(\phi)$ (shown in red). The latter signal form is also called AIT signal. The naming nomenclature underlines the geometrical form of such nonlinear EM springs regarding the ϕ / $\tau_S(\phi)$ diagram in Fig. 1 C. The EM spring is active in the interval from γ_- to γ_+ angle and the instable point shown here in the origin at zero, marked also as γ_0. Exemplarily the maximum torque is shown with τ_{max} occurring at angle γ_{max}. By using classic EM theory, it is shown that such AIT signals arise out of magnetic attraction and repulsion using moving 2D and 3D current loop structures.

Two calculation flaws could be found in a previous attempt to describe purely analytical AIT signals [10], that claimed also an energy excess in MEH systems based on approaches in [1, 2]. Validation of AIT signals is a key step for further research activities, which will be, most prominently, investigation of the energy source.

AIT signals can be analytical generated using Maxwell Stresstensor calculations and approximation models using Fourier Series [9], [11] as well as other approaches shown in [12].
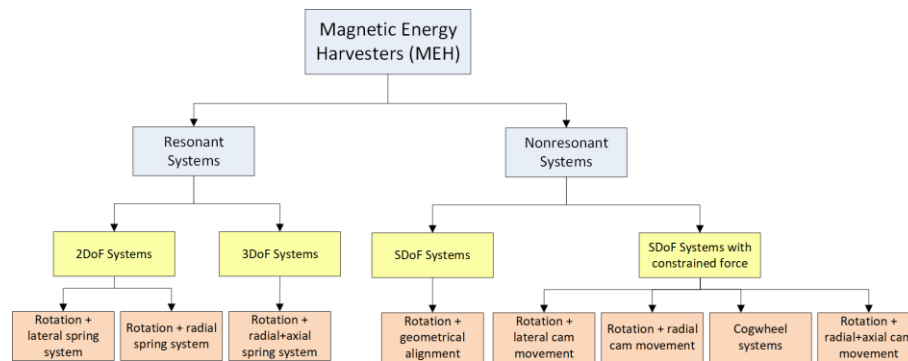

Fig. 2. Classification of MEH systems

Fig. 2 shows some common system configurations that are suitable for transferring magnetic energy in mechanical energy. In the category 'Resonant Systems', multi degree of freedom systems are shown that exhibit most interesting resonant phenomena. In the first subcategory '2DoF Systems', a rotational DoF coupled with an axial DoF can exhibit parametric resonance, described first in [9] and might be also a model for [8]. Instead of a lateral movement, also a radial movement can be envisaged exhibiting similar resonances as shown in [8]. Also, conceivable is a system with two rotational DoF's in series, where both DoF's are coupled by torsion PM springs. Another possible system, shown in the subcategory '3DoF Systems' could have more than 2DoF's, in which a more complex resonance synchronization process is in place. In the category 'Nonresonant Systems' a plethora of possible MEH system-geometries can be envisaged. The first subcategory 'SDoF Systems', the geometry of the PM spring is crucial to create AIT signals. Attempts by the author to create and measure such systems failed. A second subcategory ('SDoF Systems with constrained force') carries SDoF systems with constrained force(s). In the latter belongs also a system with rotational- and a constrained lateral-movement, as presented in [11] as well as a cogwheel system shown in [12]. Another simple MEH system, has a radial constrained force which is modeled and validated in this manuscript.

Validation of AIT signals are challenging when using two degree of freedoms or a single degree of freedom system with a constrained force, as the mechanical precision for manufacturing the parts is higher and mechanical friction is higher than using a simple SDoF model without constraining force (Appendix E.). It is of great help to find suitable PM structures and trajectories using an analytical model.

II.   Modeling PM Situation

2.1 General remarks of PM modeling

A common practice is to model a PM with one or several filamentary DC current loops. In such a model, mutual inductance between the current loops is not considered. The simplest PM to model is a circular filamentary line, e.g., one single current loop. The second simplest structure is a cylindrical shell (a 3D structure; A1 of Fig. 1, A1, shown with three current loops) or a flat disk (a 2D structure; Fig. 1, A2, shown with two current loops). Another geometrical structure that can be modeled is a cylinder PM (a 3D structure; Fig. 1, A3, shown with three current loops) as well as many other shapes.

All shapes considered in this investigation are based on circular current loops with a uniform

current density. All examined shapes were modeled with a realistic shape structure, that exhibit a **B**-field which can be created by superposing multiple, of the shelf commercialized, PM structures. The force or torque of two PMs can be calculated using Lorentz force law

$$\mathbf{F_{mag}} = q\big(\mathbf{E} + (\mathbf{v} \times \mathbf{B})\big) \cong q(\mathbf{v} \times \mathbf{B}) \tag{II.1}$$

where $\boldsymbol{F_{mag}}$ is the resulting force, **E** the electric field-, **B**-the magnetic field- and **v** the point charge q velocity trajectory-vector. As in these MEH systems, velocities are extremely low in respect to the speed of light, **E** can be disregarded (which is always assumed in calculations for electrical machines, see for instance [13]). Generally, magnetic forces will do no work (Q_{mag}) on isolated electric charges [14], since

$$Q_{mag} = \int \mathbf{F_{mag}} \cdot d\mathbf{l} \xrightarrow{d\mathbf{l} = \mathbf{v_0}\, dt} \int q(\mathbf{v} \times \mathbf{B}) \cdot \mathbf{v_0}\, dt = 0 \tag{II.2}$$

the result in Equation (II.2) follows when **v** and the created path velocity vector $\mathbf{v_0}$ are equal, which is always the case using a point charge. However, for the PM-based MEH systems proposed in this paper, we show that the calculated total magnetic work Q_{mag} is unequal zero by applying a (a) well-deliberated closed trajectories Γ and (b) instead of a point charge, an extended area or volume charge (see current loop structures of Fig. 1, lhs, A1…3). So, in contrast to equation (II.2),

$$Q_{mag} = \oint_{\Gamma} \mathbf{F_{mag}} \cdot d\mathbf{l} \neq 0 \tag{II.3}$$

This result is validated by simple experiments shown in detail in chapter IV.

2.2 Analytical static torque modeling

In this section, all equations are presented to generate the analytical torque and energy signals using fundamental EM theory. These equations are applied on basic PM structures simulated in chapter III and validated in chapter IV.

2.2.1 Structure of the modeling setup

Modeling setups for two basic PM geometries in Cartesian coordinates are shown in Fig. 3. Both structure setups have the same nomenclature and show principally the same model. The only difference is the number of circular current loops for modeling the stator PM (called primary loops shown in blue) and the geometrical shape of the rotor PM (called secondary loops shown in green) formed with a different alignment of circular current loops. The center of each primary loop is called $C_{P1,2,...,n}$, with the PM structure center of mass location at $x = 0$, $y = yP$ and $z = 0$ of the reference frame origin C_0 (assuming all primary current loops form one rigid stiff body).
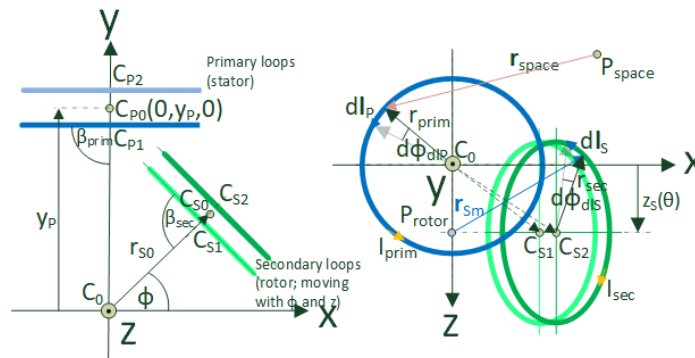

Fig. 3. Modeling and nomenclature situation Setup

The secondary loops are placed at $C_{S1,2,...,n}$, forming a 3D structure (Fig. 3). The secondary (rotor) loops are rotating in the x-y frame (center of rotation at P_{rotor}) with angle ϕ and might move translatory with a cam movement z_{CAM} of

$$z_{CAM}(\theta) = z_O + z_A \sin(\theta + \xi_O) \tag{II.4}$$

having an offset angle ξ_O, an offset distance z_O and a harmonic amplitude z_A (see also Fig. 1, B, where degrees of freedom are shown in red as ϕ, r and z). The angle θ moves synchronously with the rotor rotation angle ϕ ($\theta = \phi$) or a radial (in plane) movement like

$$r_{CAM}(\theta) = l_{PM} + \frac{l_0 \cos\left(\theta - arcsin\left(\frac{l_e}{l_0}\cos(\theta)\right)\right)}{\cos(\theta)} \tag{II.5}$$

Such a radial cam is a rotating piston like movement, see also lumped parameter model Fig. 5. where l_e denotes the eccentricity (crankshaft radius), l_0 the rotor lever, l_{PM} the rotor piston extension and

angle θ, a synchronously moving rotor rotation angle ϕ ($\theta = \phi$).

Validation has been done with radial movement (II.5) and a used approximation function [15] (see also Appendix A.) as such radial cam generates much larger AIT signals. In chapter 3.2-3.4 three analytical cases will be discussed, all of them forming cylindrical shells. Such a situation is shown in Fig. 3, using several primary and secondary current loops, forming a stator, respectively rotor PM).

A ring vector segment on the primary loop with angle ϕ_{dlP}, radius r_{prim} is named dl_P and the flowing current I_{prim}, both looking in the same direction. For the secondary loops, the nomenclature is given accordingly ϕ_{dlS}, r_{sec}, dl_S and I_{sec}, considering that all secondary loops carry the same current, dl_S and I_{sec} are pointing in the same direction. A point in space P_{space} at distance r_{space} from vector dl_P is shown for illustration purpose. Radius from P_{rotor} to C_{S0} is named r_{S0} and vector from P_{rotor} to a dl_S segment is $\boldsymbol{r}_{Sm}$ (shown in Fig. 3 and Fig. 4).

2.2.2 *Magnetic flux density created on primary loop(s)*

The magnetic flux density vector $\boldsymbol{B}_n$ (index *n* designates the secondary ring $n = 1, 2, ...$) at any point in space $\boldsymbol{P}_{space}$ with vector length $\boldsymbol{r}_{space}$ created by one primary loop can be obtained using Biot-Savart, equation (II.6a), permeability of free space designated as μ_0).

$$\boldsymbol{B}_n = \frac{I_{prim}\,\mu_0}{4\pi} \int \frac{dl_P \times \boldsymbol{r}_{space}}{|r_{space}|^3} \tag{II.6a}$$

$$\boldsymbol{B}_{prim} = \sum_n \boldsymbol{B}_n \tag{II.6b}$$

Using the superposition principle and cumulating all vector field points by applying equation (b) results in the final stator PM flux density vector $\boldsymbol{B}_{prim}$. To calculate numerically ($dl_P \to \Delta l_P$) this field at the points in space that are on the secondary loops, an integration approach has been realized using an averaging method. By integrating clockwise all $\Delta \mathrm{B}_{prim(cw)}/2$ elements and counterclockwise the same number of $\Delta \mathrm{B}_{prim(ccw)}/2$ of the primary loops to obtain the final averaged flux density of equation (b) for any point in space $\boldsymbol{P}_{space}$. These points $\boldsymbol{P}_{space}$ will be chosen for this application on all points of one or several secondary loops (two such points $\boldsymbol{B}_{S1,2}$ shown exemplary in Fig. 4).

2.2.3 *Created force on secondary loop(s)*

The total force created on all secondary loops can be obtained using

$$d\boldsymbol{F}_{Sm} = \sum_n I_{sec\,n}\,dl_{Sn} \times \boldsymbol{B}_n \tag{II.7a}$$

$$\boldsymbol{F}_{Sm} = \int_0^{2\pi} d\boldsymbol{F}_{Sm} \tag{II.7b}$$

In equation (II.7a) the sum delta force $d\boldsymbol{F}_{Sm}$ is calculated for all cumulated delta force segments $d\boldsymbol{F}_{S1,2,...,n}$ that form the rotor structure, see also Fig. 4. In Equation (b) all cumulated force segments are integrated over the rigid body circumference from 0 to 2π. Again, the implementation makes use of the same numerical averaging method as for calculating Equations (II.7a) and (b) (integrating clockwise all $\boldsymbol{F}_{Sm(cw)}/2$ elements on the rigid body ring and counter clockwise the same number of $\boldsymbol{F}_{Sm(ccw)}/2$ to obtain the final averaged force equation (b) in the center of gravity of the rotating rigid body). This averaging method is well suited to calculate any desired number of secondary loops of such a modeling setup. The calculated total force- and torque-signal are independent of the order, in which the secondary loops are calculated (with length of $\boldsymbol{r}_{S1,2,...,n}$).

2.2.4 *Created torque on secondary loop(s)*

Fig. 4 shows a calculation extract detail of our calc. situation while calculating equation (II.8a) depicting also the vector $\boldsymbol{r}_{Sm}$ from rotor origin $\boldsymbol{P}_{rotor}$, which moves on the z-axis with eq (II.4) or radial with eq. (II.5) to the center of contact to $\boldsymbol{B}_{Sm}$ of the rigid cylindrical 3D ring (Fig. 4). The rotating reference frame with origin C_{S0} is shown in Cartesian coordinates (x' and z'), the rigid body with limits r_{S1} and r_{S2} is shown as well as the global reference frame with origin C_0. For n circular loops (n>1) in the limits of r_{S1} to r_{S2} the point of contact is in the center of gravity of all considered loops, formed by $d\phi_{dlS}$, dl_{S1} and dl_{S2} (shown in light orange of Fig. 4).
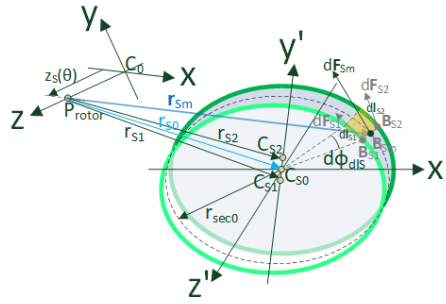
Fig. 4. Detail of torque contact point

The torque on one or several secondary loops is calculated using the (cumulated) force delta $d\boldsymbol{F}_{Sm}$ in equation (II.8a) using the same averaging method as for the $\boldsymbol{B}_n$ and $\boldsymbol{F}_{Sm}$ calculation. The total torque $\boldsymbol{\tau}_{Sm}$ created on all secondary loops can be obtained from

$$d\boldsymbol{\tau}_{Sm} = \boldsymbol{r}_{Sm} \times d\boldsymbol{F}_{Sm} \tag{II.8a}$$

$$\boldsymbol{\tau}_{Sm} = \int_0^{2\pi} d\boldsymbol{\tau}_{Sm} \tag{II.8b}$$

Note that $\boldsymbol{r}_{Sm}$ will always have the same length, as we assume to deal here with a rigid body. The resulting torque signal is calculated simultaneously with the force signal and the order in which each ring delta force segment $d\boldsymbol{F}_{S1,2,...,n}$ is added up does not matter. Instead of calculating the resulting torque signal simultaneous with the force signal, it could be calculated once the force signal of each current ring $\boldsymbol{F}_{Sn}$ is known using

$$\boldsymbol{\tau}_{Sm} = \boldsymbol{r}_{S0} \times \sum_n \boldsymbol{F}_{Sn} \tag{II.9}$$

For both calculation methods (II.8a), (II.8b) or (II.9) to generate the resulting torque signal $\boldsymbol{\tau}_{Sm}$, the order in which each nth secondary current loop is added up does not matter. Using Equation (II.9), the approach of [10] is made, which is only an approximation for force and torque calculations and therefore not suitable for energy considerations. Calculating torque signals using permanent magnets, the findings of [16] are also of interest.

2.2.5 Energy considerations

There are three energy components, the rotation of the rotor ϕ as well as the translatory rotor-components r and z (compare Fig. 1, B). For the rotary movement component, the energy to consider is

$$Q_\phi = \int_0^{2\pi} \tau_Z d\phi \tag{II.10}$$

For the translatory z_{CAM} movement component, eq. (II.4), the relevant energy is

$$Q_Z = \int_0^{2\pi} F_Z z_S(\theta) d\theta \tag{II.11}$$

For the radial r_{CAM} movement component, eq. (II.5), the relevant energy is

$$Q_R = \int_0^{2\pi} F_R r_S(\theta) d\theta \tag{II.12}$$

The total energy becomes

$$Q_{tot} = Q_\phi + Q_R + Q_Z \tag{II.13}$$

Units of all energies $Q_{\phi,R,Z}$, Q_{tot} are given in Joule if not otherwise noted.

2.3 Analytical dynamic torque modeling

In this chapter we are modeling by means of a lumped parameter model the dynamic situation of a rotor with a radial cam, creating an AIT signal. Fig. 5 shows the most prominent components of the lumped parameter model (stator elements not shown). The rotor consists of three parts: rotor base inertia J_r (rotor plus stroke bearing rail), rotor carriage (PM, PM-fixation and -carrier) with mass m_c plus plunger with J_p to move rotor carriage m_c with reduced radius r_c (center of gravity of all m_c components) in shown cam trajectory (eq. (II.5) red dot dashed through the rotor PM center of gravity). Trajectory of the reduced point mass of the rotor (shown as radius $r_c(\phi)$ and point of gravity for current carriage position as P_r) shown in orange. Rotor frictions consist of rotor bearing friction D_b, stroke bearing friction D_s and plunger friction bearings $D_{f1,2}$. Dynamic torque sensor consists of two inertias $J_{1,2}$ and a stiff torsion

spring of $C_s = 100 Nm/rad$ for measuring the rotor torque. Flipping point angle in ground view shown as γ_0.
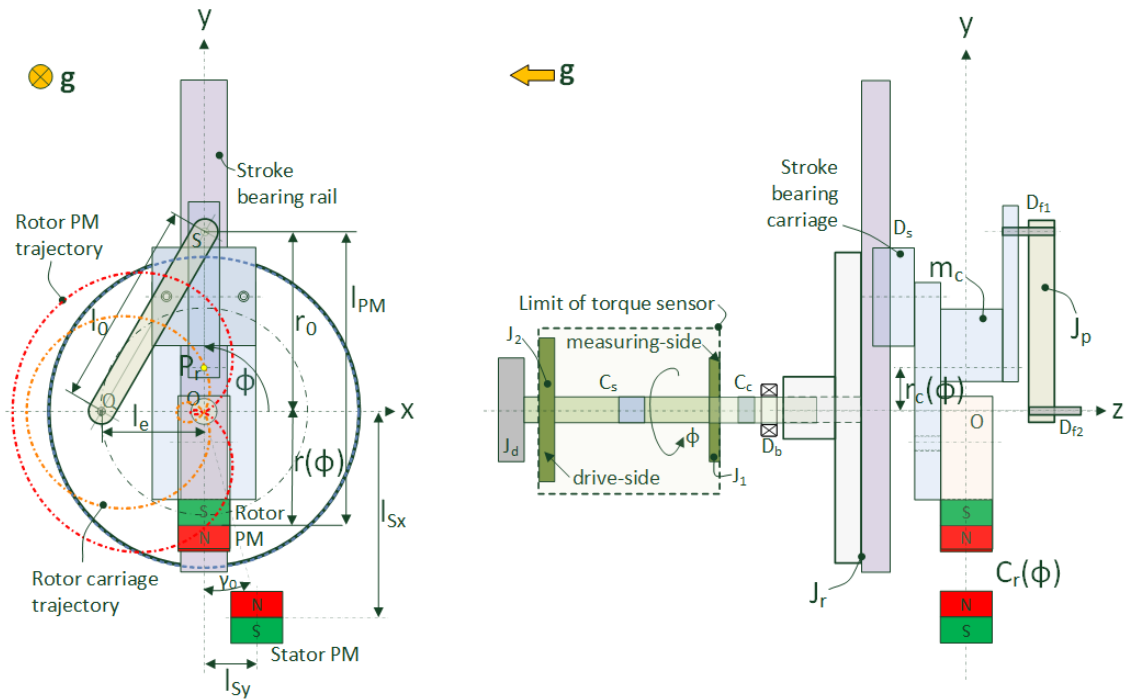

Fig. 5. Lumped parameter model in ground view (lhs) and profile (rhs)

Coupling between torque sensor and rotor structure is $C_c = 980 Nm/rad$. The nonlinear stiffness created by the rotor PM trajectory and stiff fixed stator PM is denoted as $C_r(\phi)$. On the drive side of the torque sensor, J_d represents the drive inertia, a small lever which is carried with a pusher dog in the instable position. The sensor inertia J_1 contributes also to the total inertia measuring side ($<1\%$) and J_2 (approximately 15%; drive side).

Considering a single DoF system with freedom ϕ, the torque DE for such a system can be derived with the Lagrange method. It follows, having an arbitrary continuous cam function f_r in the center of gravity of the moving mass m:

$$(f_r(\phi)^2 + f_r'(\phi)^2) \, m \, \phi'' + \left(f_r(\phi) + f_r''(\phi)\right) f_r'(\phi) \, m \, \phi'^2 + D(\phi') \, \phi' + C(\phi) \, \phi = 0 \qquad \text{(II.14)}$$

The nonlinear friction is denoted with $D(\phi')$ as well as the nonlinear spring function given as $C(\phi)$. Applying eq. (II.14) to our system and replacing the radial cam function with an approximation function with error $<2\%$, see [15] and additional information in the Appendix A., it follows:

$$J_{tot} \, \phi'' + \left(\frac{l_e^2}{l_0^2}(\cos\phi)^2(l_0 + l_e\sin\phi)^2 + \left(l_{PM} + l_e\left(1 - \frac{l_e}{2l_0}(\cos\phi)^2 + \sin\phi\right)\right)^2\right)m_c \, \phi'' + $$

$$\frac{l_e}{4l_0^2}\cos\phi\left(-l_e^2 + 4l_0\,(l_e + l_{PM}) + 3l_e^2\cos 2\phi\right)(l_0 + l_e\sin\phi)\,m_c\,\phi'^2 + D(\phi')\,\phi' + C(\phi)\,\phi = 0 \qquad \text{(II.15)}$$

The total inertia that needs to be accelerated in the system is $J_{tot} = J_d + J_2 + J_1 + J_r + J_p$ plus the rotor carrier with mass m_c (and reduced radius r_c in the center of gravity of this radial moving mass shown on the rhs of Fig. 5), the total friction torque with a nonlinear friction model [17] to overcome shown as D (consisting of $D_b + D_s + D_{f1,2}$) and the generated torque due to the nonlinear spring torque $\tau_s = C_r(\phi) \, \phi$. No analytical solution could be found for (II.15). A general solution could be generated by a linear piecewise approximation of the spring signal when considering only viscous friction, see also [18]. This exercise is not done, and only numerical simulations are presented (chapter III, IV) using several nonlinear solvers such as ode23 or ode45.
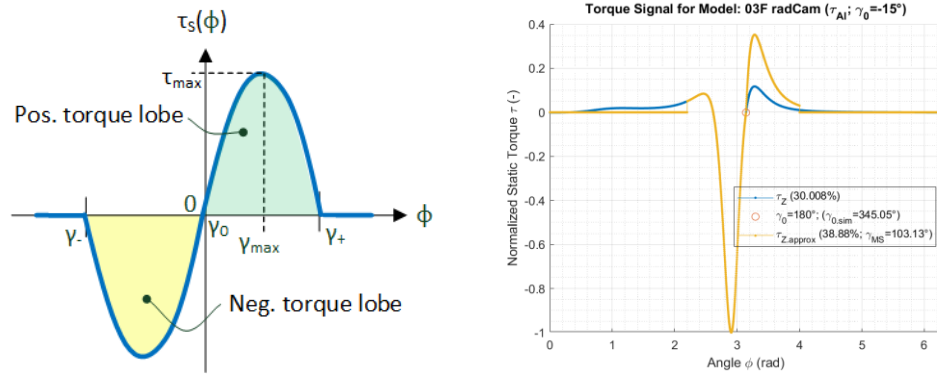
Fig. 6. Energy considerations in nonlinear EM-torque springs exerting commensurable (lhs and rhs, blue line) and incommensurable (rhs, red line) signals

The unstable (flipping) point γ_0 is shown in Fig. 6 lhs again in the origin. This point γ_0 on the trajectory of the rotor, where the stator exerts no torque on the rotor, determined by the geometry of the stator- and rotor-PM, which is often also the closest PMs rendezvous point. Such a nonlinear symmetric EM spring is in detail treated in [15, 18, 19]. Note that the received energy from the neg. torque lobe (yellow area) is released in the pos. torque lobe (green area) or vice versa. Fig. 6, rhs, shows two normalized nonlinear asymmetric incommensurable τ_{AI} signals (orange line represents an adapted version for the validated torque signal in chapter IV, and the original τ_{AI} signal, blue line from the simulation, chapter 3.4). Its spring incommensurability in percentage is shown in brackets (50% meaning a commensurable signal – same area above and below the ϕ-line). The commensurable torque signal has been artificially enlarged in the positive area to meet the measured torque signal on the shaft. Note also that the trajectory of a rotor in this setup is none uniformly accelerated (see also Appendix A.), and we deal with nonlinear friction. Considering the system dynamically, the max. ang. velocity ϕ' is reached at the point $\phi = \gamma_+$ or at $\phi = \gamma_-$. Due to the applied friction model in combination with the shape of the spring signals (see Fig. 7), the max. ang. velocity at $\gamma_{-,+}$ should only significantly vary ($> 0.5 rad/s$) if we deal with an incommensurable EM spring.

III. Simulations

The discussed equations from chapter II are applied to find in some structures' energy excess when using SDoF systems without and with a constrained force, such as (II.4) or (II.5).

3.1 Simulation parameters

Simulation parameters are shown in Table 1, Table 2 and Table 3. All symbols except for iteration parameters are depicted in Fig. 3, Fig. 4. Distance from the center of reference to each (primary) current loop is denoted with $y_{P1,2}$.

Table 1 Parameters of the modelled system (chapters 3.2-3.4)

Symbol	Value	Unit	Description
μ_0	$4\pi\ 10^{-7}$	Vs/Am	Permeability of free space
I_{prim}	-1000	A	Current primary loop
I_{sec}	$+1000$	A	Current secondary loop
r_{prim}	5	mm	Radius primary current loop
β_{prim}	90	$°$	Tilting angle prim. loop
β_{sec}	90	$°$	Tilting angle sec. loop
$y_{P1,2}$	$31,35$	mm	Distance to center of 1st, 2nd primary loop
n_{PS}	50	$-$	# of primary and secondary loop steps
n_ϕ	3600	$-$	# of simulated rotor revolution angles

First iteration parameter n_ϕ sets number of steps for one rotor revolution and second iteration parameter n_{PS} is used to calculate number of points for the **B**-field point calculations emitted by the primary loop, e.g. number of Δl_P and $\Delta\phi dl_P$'s using Equations (II.6a) and (b) and number of rotor angle steps $\Delta\phi dl_S$ for the force and torque calculations on secondary loop(s) equations (II.7a), (b) and (II.8a), (b). Note as averaging takes place for n_{PS} using clockwise and counterclockwise integration steps, n_{PS} is in fact doubled (once started at 0 and once at 2π). Using such an averaging method improves the

convergence to stable force (**F**), torque ($\boldsymbol{\tau}$) and energy (Q) signals. All following simulations are using values indicated in Table 1-Table 3 unless otherwise noted.

Table 2 Parameters for axial cam (chapter 3.3)

Symbol	Value	Unit	Description
z_o	5	mm	Offset position cam
ξ_o	0	°	Offset angle cam
z_A	10	mm	Amplitude cam

Table 3 Parameters for radial cam (chapter 3.4)

Symbol	Value	Unit	Description
l_e	19.75	mm	Eccentricity
l_0	40	mm	Lever length
l_{PM}	-60.8	mm	Offset distance to rotor PM center

In Table 2 and Table 3 additional parameters for cam data are given. Table 2 defines an axial cam, a forced movement into the z-axes using eq. (II.4) and Table 3 defines parameters for a radial cam (shown in Fig. 5 as PM rotor trajectory) using eq. (II.5). Note that from the given tables the created airgap between stator and rotor current loops is kept intentionally large (in the following chapters 3.3, 3.4 and 3.4 it is kept above 4mm) to avoid simulation artifacts caused by discontinuities.

3.2   SDoF systems without constrained force

In this chapter, two simulations of SDoF System without constrained force are discussed, having five circular current loops (with 2mm distance to each other) on stator and rotor each (Fig. 7). Circular trajectory radius $r_{traj} = 40mm$ in red. Center of gravity of rotor and stator loops in the xy-plane, keeping a minimal airgap of $h_{air} = 5mm$. Rotor and stator structure building a stair-like configuration with x-offset of $r_{S,PoffsetX1\ldots5} = -4, -2, \ldots, 4mm$ and y-offset of $r_{S,PoffsetY1\ldots5} = -10, -5, \ldots, 10mm$ (Fig. 7, rhs); rotor structure in Fig. 7, lhs forming a circular shell.
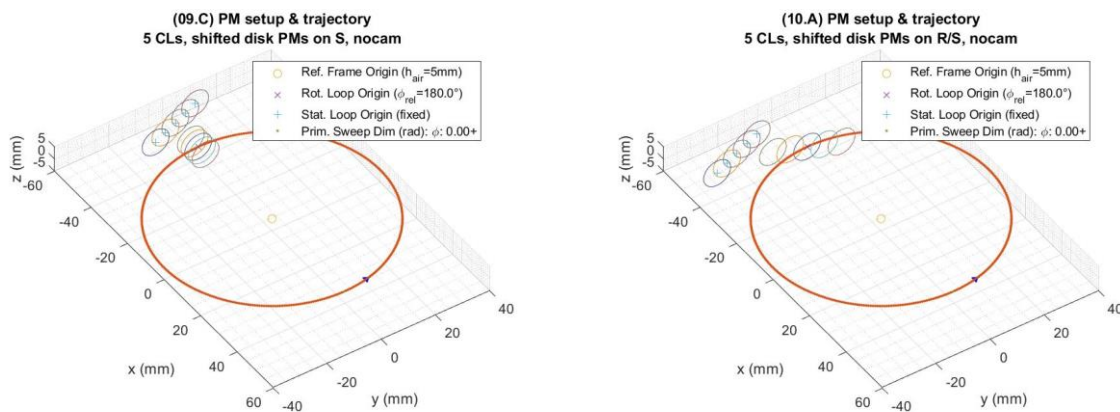

Fig. 7. Simulation setup of stair-like configured circ. current ring PM structures on stator and rotor with circular rotor trajectories (in red)

On the lhs of Fig. 8 the resulting torque is depicted, creating a seemingly realistic asymmetric torque of 4.9% (see also [9], [11], [20]) and 0% respectively. Note, that we have no cam applied and no z-offset for the rotor trajectory on P_{rotor}, no z-force is generated. On the rhs of Fig. 8 the resulting energy output is shown which accumulates to astonishingly $Q_{totC} \cong 1320\mu J$ and Q_{totC} close to zero respectively (case of straight rotor shell). The energy outcome of a structure like 09.C is very close to zero (also considering DC current loops of 1kA each) and a torque $\boldsymbol{\tau}_{SC}$ is generated. Note, that if stator is moved to out of y_S to $y_S = -20mm$ (same situation as structure 10.A, also a torque $\boldsymbol{\tau}_{SC}$ would be generated. In earlier experiments, such structures where measured and the shown torque could be validated statically. However, the important dynamic validation gave a too weak/no AIT signal and could not be successfully validated, see also Appendix G.
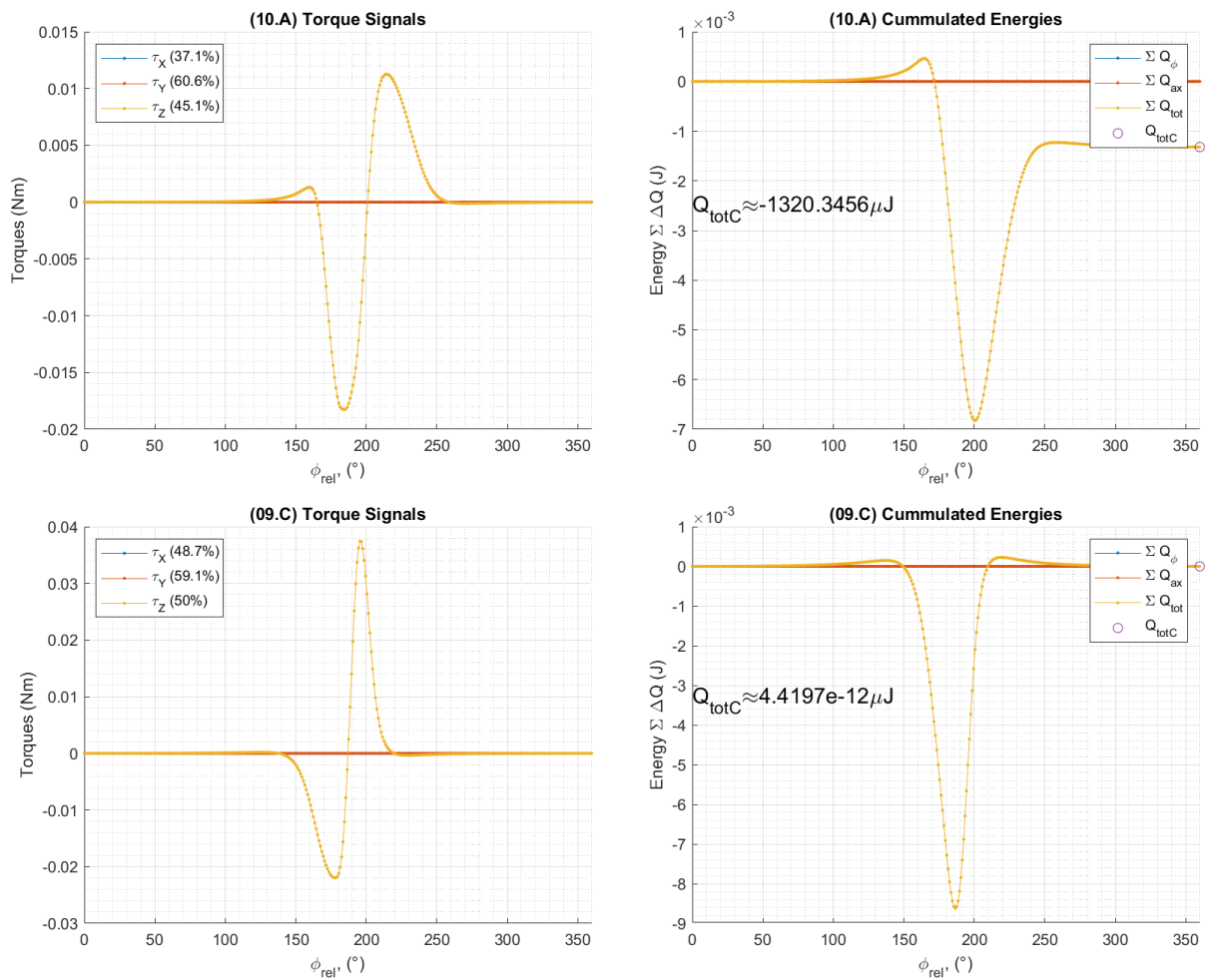
Fig. 8. Calculated torque (lhs) on rotor and energies (rhs) for shown setups in Fig. 7

3.3   SDoF systems with constrained force (axial cam)

In this chapter, a simulation of a SDoF system with constrained force is discussed using a cam described by eq. (II.4) perpendicular to the rotating rotor plane (axial). Each stator and rotor PM consists again of 5 circular current loops (Fig. 9) with the same x-spacing between each loop as in previous setup of chapter 3.2. A stator rotor PM rendezvous of two cylindrical shell PMs are shown when rotor has moved 180° from the start position. The cam trajectory of the rotor with z- and rotating offset ξ, and amplitude is given in Table 2. The dashed blue line is the projected circular orbit in the x-y plane. Fig. 9 shows the setup (lhs), the resulting torque (middle) and the resulting energy output (rhs) over one revolution. Energy accumulates to $Q_{totC} \cong 113\mu J$. No experiments have been done with such structures.
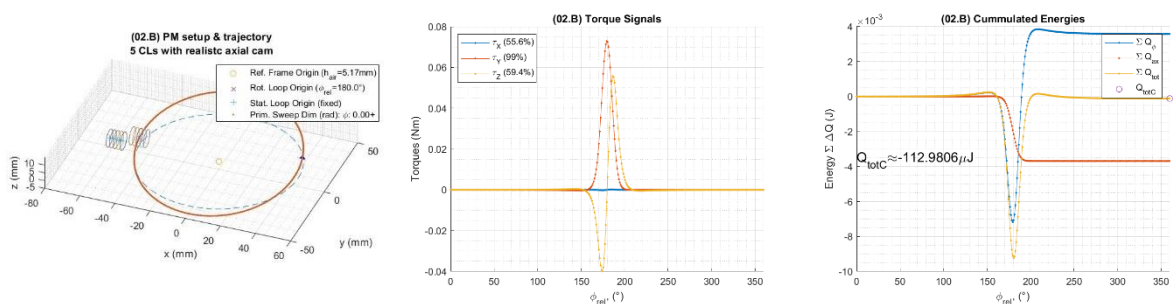
Fig. 9. PM setup of with circular shells of stator and rotor and an asymmetric placed cam trajectory (in red) with cam parameters shown in Table 2 (lhs); calculated torque (middle) and energies (rhs)

3.4   SDoF systems with constrained force (radial cam)

In this chapter, simulations of a SDoF system with constrained force are discussed using a cam described by eq. (II.5) in the rotating rotor plane (radial). Each stator and rotor PM consists again of 5 circular current loops (Fig. 10) with the same setup as in chapter 3.3.
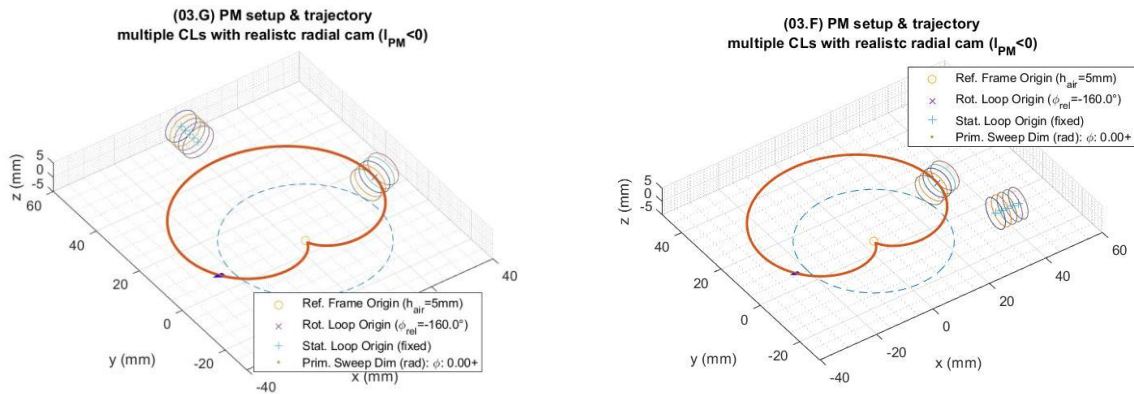

Fig. 10. Setup of circular stator and rotor PM structures and symmetric placed stator (config. 03.G, lhs) and an asymmetric placed stator (config. 03.F, rhs) with the same cam trajectory (in red); cam parameters in Table 3
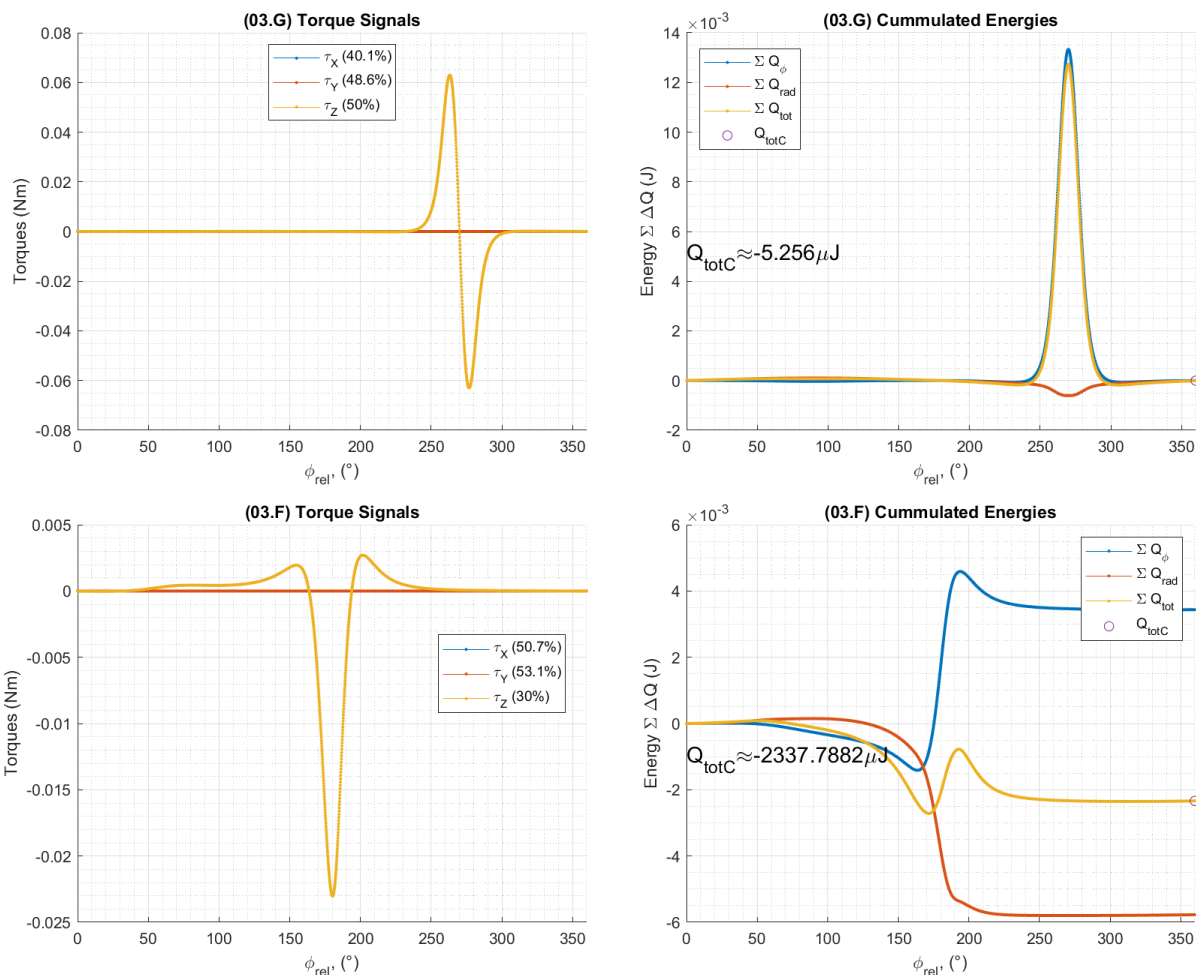
Fig. 11. Calculated torque (lhs) on rotor and energies (rhs) for setups shown in Fig. 10 (lhs and rhs)

Two simulations are shown in Fig. 10 – simulation 03.G which generates a symmetric commensurable torque signal and one 03.F with an asymmetric incommensurable torque signal. Cam trajectory is shown in

red (cam parameter in Table 3 and eq. (II.5)), and the blue dashed circle shows a circular trajectory of $r = 25mm$. The rotor PM structure's main axis is facing the simulation reference point marked as 'o'. The rendez-vous position γ_0 (instable point, compare also Fig. 6) is in 03.G on the y-axis, in 03.F at ca. 194° (compare torque signal in Fig. 11). Note that the developed torque signal for such a trajectory has an additional instable point close to 160°. It is only weakly measurable, as it is outside the two main torque lobes (see chapter IV). On the lhs the developing torque signal is shown; configuration 03.G creates a commensurable symmetric torque signal (compare also with [18]) and configuration 03.F creates a strong asymmetric incommensurable torque signal. The resulting energy output is shown which accumulates for configuration 03.G close to zero ($Q_{totC} \cong 5\mu J$) and in config. 03.F to $Q_{totC} \cong 2338\mu J$.

3.5 Dynamic simulations of SDoF systems with constrained force

Simulations are shown applying model equation (II.15) in the system setup of chapter 3.4. Such SDoF systems carry in this simulation experiment one PM torque spring of the form $\tau_s = C_{nl}(\phi) \cdot \phi$ using asymmetric commensurable ($\tau_s = \tau_{AC}$) and income-mensurable ($\tau_s = \tau_{AI}$) torque signals. (In Appendix E. , simulations are shown with a true SDoF system, without constrained force.) For shown simulations, the lumped parameter in Fig. 5 applies (chapter 2.3), with parameter set: $m_c = 47.2g$, and radial cam (II.5) into point of gravity of radial moving carriage mass m_c with parameters $l_e = 19.8mm$, $l_0 = 40.0mm$ and $l_{PM} = -26.0mm$ (orange trajectory in Fig. 5). All elements forming inertia results to $J_{tot} = 6.5 \, 10^{-5} kg \, m^2$ using a nonlinear friction model [18] and nonlinear spring $C_{r.max} = 0.06 \, Nm/rad$ of the form shown in Fig. 6, rhs. In Fig. 12 and Fig. 13 the negative (lhs) and positive (rhs) flipping from the instable point (γ_0) of ϕ with initial start condition ϕ_{s+} and ϕ_{s-} close $\gamma_0 \cong 90°$ (Fig. 12) and close to $\gamma_0 \cong -14°$ (Fig. 13), see also markers '*'. The same signals are depicted in each figure: the motion signals ϕ (path) and ϕ' (its ang. velocity) and the nonlinear spring signal T_{mag}. Markers, 'o' show the first max. and min. ang. velocity after starting a flip. The pink torque signal is shown normalized – max. breaking torque represents mentioned $C_{r.max}$.
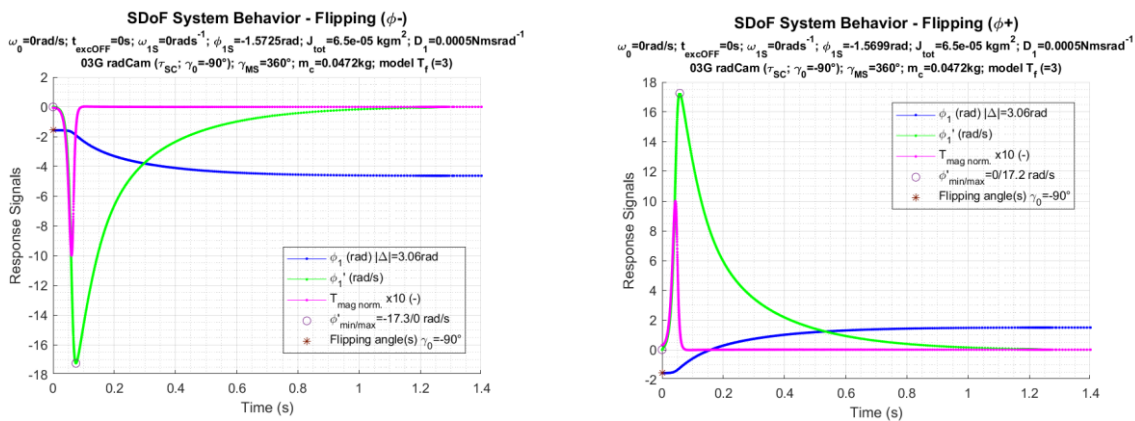

Fig. 12. Nonlinear symmetric commensurable torque spring in config. 03.G (see Fig. 10, lhs)
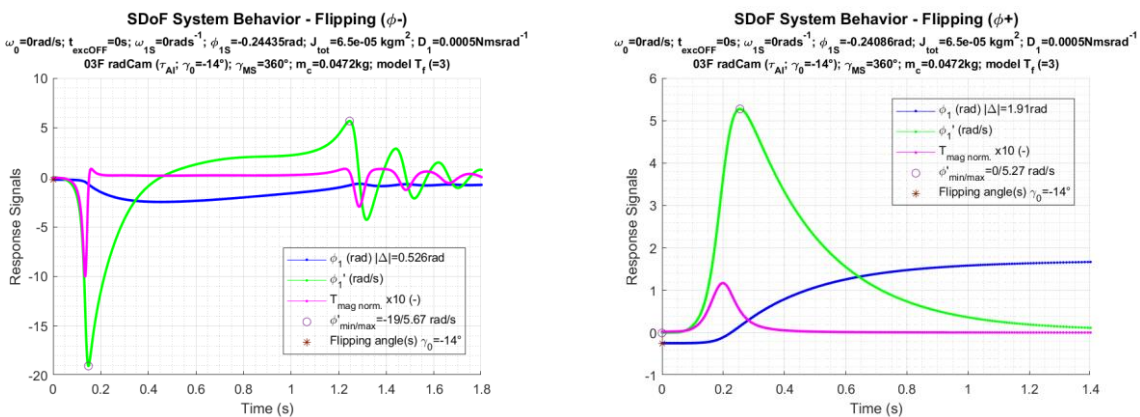

Fig. 13. Nonlinear asymmetric incommensurable torque spring in config 03.F (see Fig. 10, rhs)

In Fig. 12, flipping by using (symmetric) configuration 03.G is depicted. A jump from the instable position γ_0 in both directions results in a perfect symmetric behavior (ignoring signs of motion signals) – as expected.

Fig. 13 shows again jumps using the ideal, simulated PM torque spring (Fig. 11, bottom left). No torque lobe amplification is used, nor a cropping of the torque spring's influence is in place, e.g., the EM torque spring is over one full revolution active, $\gamma_{MS} \cong 360°$. Such an ideal model is not realistic, compare with Fig. 6, rhs, orange vs. blue torque line, where $\gamma_{MS} \cong 103°$ and outside this angle interval the friction dominates the torque influence. For this configuration, an asymmetric behavior of the motion signals (ang. velocity in neg. flip direction is ca. 4x larger and accordingly also the path signal jump larger. Note, that due to the influence of the EM torque spring over 360°, the rotor is not coming to a standstill immediately after one single jump (in neg. direction).

IV.   Validation Measurements

4.1   Testbed

Figure 19 shows the physical model of the testbed for SDoF systems for with and without constrained force. Influence of gravitation is eliminated by lying the rotor disk parallel to the earth's surface (compare Fig. 14 and lumped parameter model Fig. 5). The central device is a high precision torque sensor with measurement torque interval of $\pm 1 Nm$ and precision of 1%. General standard tolerance of testbed is $\pm 0.1 mm$ for self-manufactured parts. The sensor is connected to an Al bellow coupling, which connects in turn the rotor-shaft and rotor system with radial cam configuration. In this testbed a rotor fork system has been created to easily test the torque signal of various rotor and stator PM structures. In the current setup, cylinder PM structures have been tested with a radial cam system, as large τ_{AI} signals can be created (compare to Fig. 10).
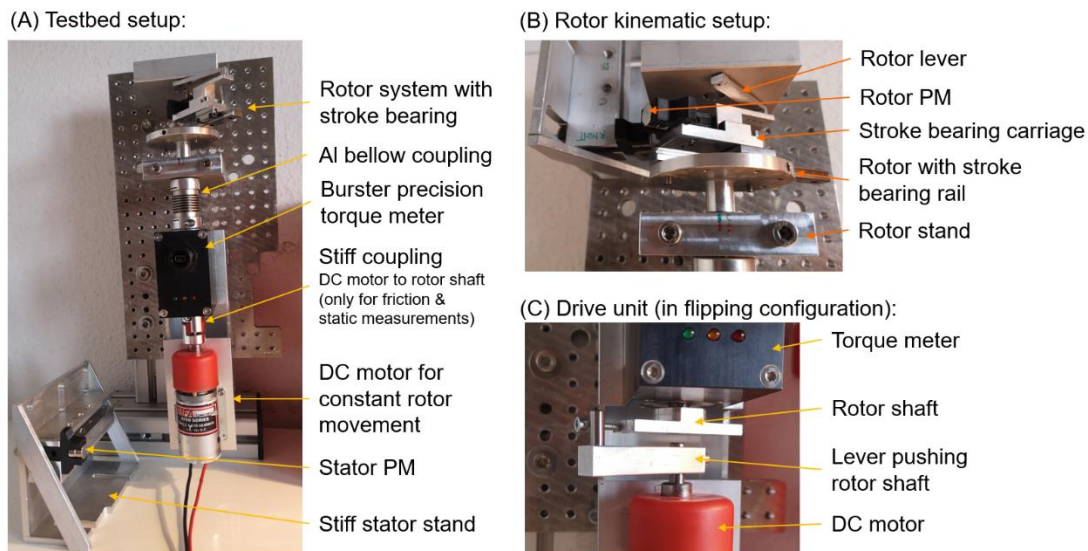

Fig. 14. Testbed in vertical measurement position for friction measurements (A); rotor kinematic with plunger and stroke bearing (B) and drive unit in dynamic flipping configuration (C)

The torque sensor has a built-in rotary encoder with 400 inc/revolution and is set up to transmit 200 samples of torque- and rotary encoder -samples per second. Three distinct tests have been made: (i) friction measurement of system (shown in (A) of Fig. 14), (ii) static torque tests by applying a constant small ω_0 on the rotor over 360° (similar to (A) of Fig. 14, but having stator stand installed as shown in detail (B) of same figure) and (iii) dynamic flipping tests by removing coupling between DC motor and torque sensor and replace it with a pushing lever (shown in (C) of Fig. 14). All tests for friction estimation, static and dynamic tests have been repeated three times, if not otherwise noted. All signals are up sampled (using interp1 and spline) for easy manipulation (precision of 0.1°), to always have 3600 datasets for one revolution available. According to the testbed measurement system, notation for revolving ϕ in positive direction is called clockwise (cw) and revolving ϕ in negative direction is called counter-clockwise (ccw).

4.2   Friction measurements

Friction tests are important to validate the shape of the nonlinear magnetic spring and have been realized to validate simulated z-torque signals (see model setup, Fig. 5). For this purpose, the torque signal

with rotor PM and installed cam kinematic without having a stator PM in place has been measured.
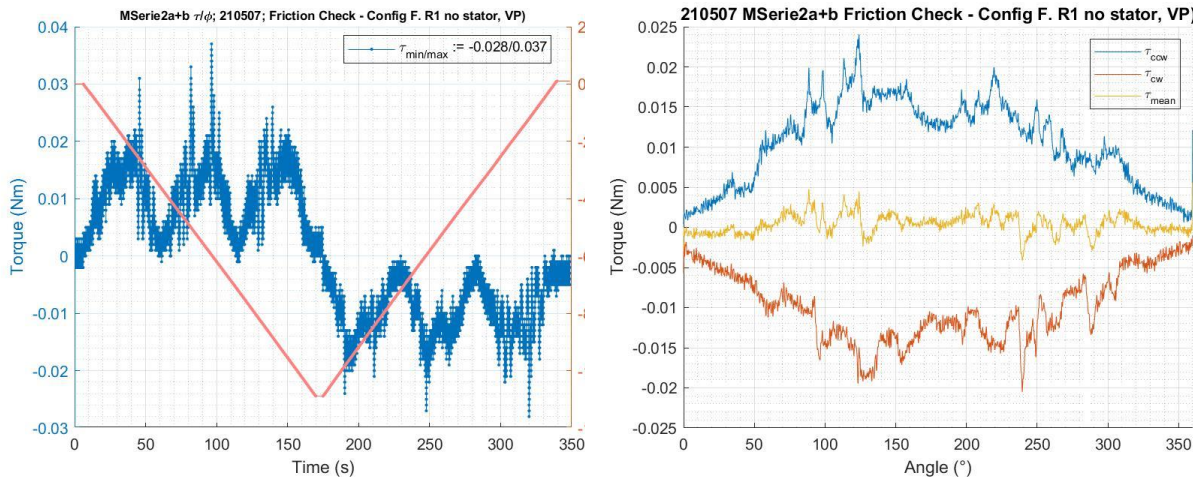

Fig. 15. Friction signals, raw data (lhr) and 3x superposed friction signal (rhs)

Fig. 15 shows the friction in this system. On the lhs the developing friction torque over 3x360° and the path signal, on the rhs the 3x averaged friction over 360°. The friction torque signal on the shaft in ccw direction (blue) and in red for revolving shaft cw; the orange torque signal shows the averaged signal $\tau_{mean} = \frac{1}{2}(\tau_{ccw} + \tau_{cw})$. It confirms the accuracy of the used torque sensor, which stays below $\pm 0.01 Nm$. System setup is configured to show at 0° the cam rendez-vous position of configure 03.G (compare Fig. 10, lhs). In this position, the ang. velocity for the rotor PM is maximal (compare, Fig. 21 and position of cam at 270°, see appendix, Fig. 20, middle).

4.3 *Static measurements*

Static tests are exercised to validate the shape of the magnetic spring. For this purpose, the torque signal has been measured by approaching clockwise (cw) and consecutively counterclockwise (ccw) each stator rotor PM rendezvous (by turning the whole rotor structure, e.g., ϕ, slowly at least from $-\gamma$ to $-\gamma$ and back to $-\gamma$ (Fig. 9). The PM rendezvous takes place in this measurement series in the proximity of ca. 90°, in contrast to the analytical simulations, where the rendezvous takes place around 180°. In all presented tests' no datasets were excluded and are presented here as measured.

The analytical torque shape is interestingly a robust approximation, which lies in the geometry of the simulated PM object: a cylindrical shell, see also remarks in [12] on PM modeling with current loops. The measurement repeatability is close to shown friction measurements (compare Fig. 15), the analytical signal follows again surprisingly well the measured reference configuration (Fig. 16, lhs). Shown data represents the 3x averaged torque in ccw (red) and cw (blue) and is averaged ccw/cw signal in orange plus the simulated signal from config. 03.G (in purple). In Fig. 16, rhs, the same signals are shown, however, ccw signal here in blue and cw signal in red. The negative torque lobe can be easily fitted, the measured positive torque lobe is clearly larger than the simulated AIT signal. With such tests no statement can be made concerning torque incommensurability, therefore dynamic tests are imperative to check the path signal and the resulting end velocity at $\pm\gamma$ after crossing the instable flipping point γ_0. Note, that the max. torque of config. 03G is almost doubled in comparison to config. 03.F. The reason lies in how the rotor and stator PM faces meet each other during rendez-vous position around γ_0. For struct 03.F both faces are perfectly parallel to each other at γ_0 (minimum airgap distance measures $l_{ag} \cong 5mm$) – creating a higher force than in struct 03.F, where both PM faces cross each other in parallel at a much larger l_{ag}.
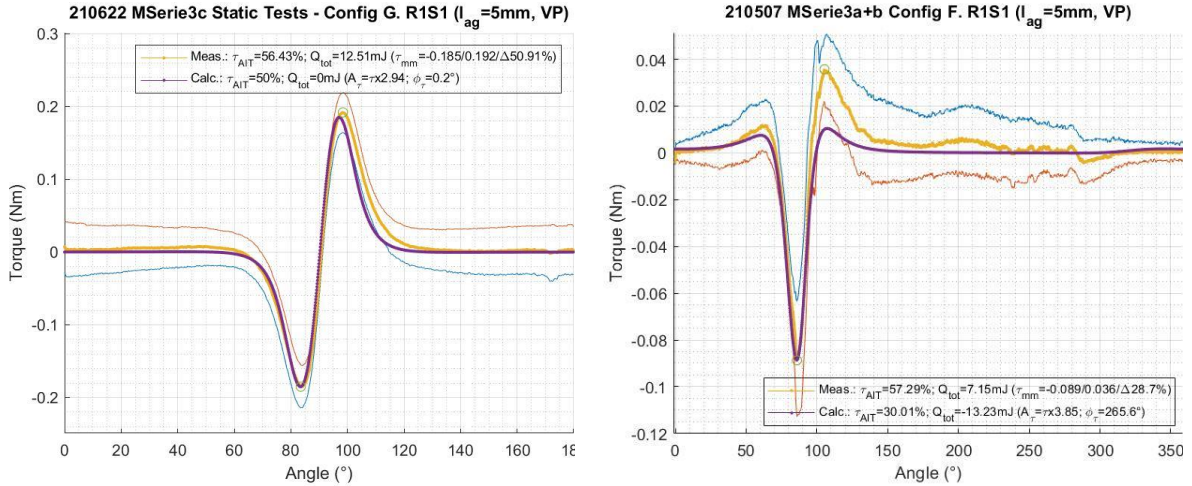
Fig. 16. Static torque signals: sym. commensurable torque reference (lhs) created by config. 03.G and asym. incommensurable torque (rhs) created by config 03.F – compare Fig. 10 and Fig. 11

4.4 Dynamic measurements

Dynamic tests are equally important as the static tests because the energy output can be estimated by measuring the angular end velocity. This velocity is generated when the rotor PM structure is accelerated while traversing the spring function from γ_0 (instable point) to $\gamma_{+/-}$ (end of EM spring function, either in cw- or ccw-direction). Fig. 17 shows a reference measurement of configuration 03.G (compare Fig. 10), using a symmetric commensurable torque signal. On the lhs, 3x times a consecutive cw- and ccw-flipping is shown (path signal in red) and developing torque signal in blue. This is achieved by configuring the drive unit with a shaft pusher (Fig. 14, detail C) that brings the rotor shaft with a small ang. velocity of $\omega_0 \cong 0.01 \, rad/s$ into the instable position. Fig. 17 rhs shows the overlayed path signals and the resulting calculated ang. velocity signals in cw (mean signal bold dashed) and ccw (bold solid lines) direction. The mean max. ang. velocities of $\omega_{mean.max} \cong 30.23 \, rad/s$ (cw-dir.) and $\omega_{mean.min} \cong -30.48 \, rad/s$ (ccw-dir.) matches well such a symmetric situation. Note that such a symmetry is also highly dependent on the manufactured testbed setup. The resulting path jump of ca. $90°$ and $-100°$ matches less. However, this is also of secondary importance, as such path jumps depend highly on the system friction, which cannot be constant in such a system with radial cam (compare Fig. 15).
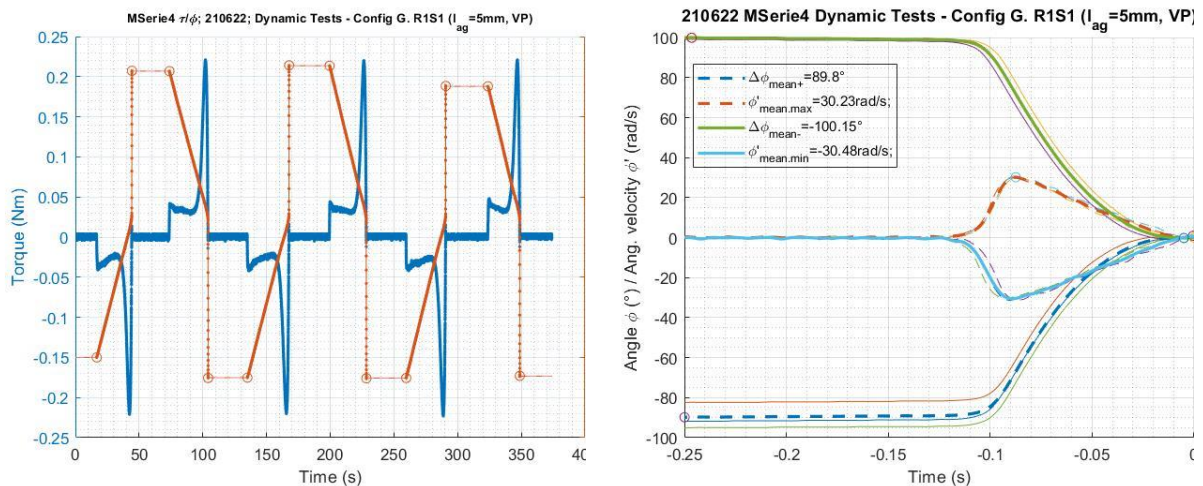

Fig. 17. Validation of a symmetric commensurable torque signal, for reference test purposes – also compare config. 03.G in Fig. 10 and Fig. 11

Fig. 18 shows the same signals as Fig. 17 – this time however using config. 03.F (compare Fig. 10, rhs) creating an asymmetric torque signal. On the lhs of Fig. 18 the measured torque (blue) and the path signal in cw direction is shown (cw and ccw direction were measured separately, see also Appendix F.). Following the same procedure as described for Fig. 17, the resulting mean max. ang. velocities of $\omega_{mean.max} \cong 10.17 \, rad/s$ (cw-dir.) and $\omega_{mean.min} \cong -18.78 \, rad/s$ (ccw-dir.) show a

clear asymmetry. This asymmetry is also reflected in the mean angle path: from γ_0 in cw dir. reaches ca. $114°$ vs. ccw dir. of $-172°$ (an angle difference of ca. $58° \equiv 1rad$).
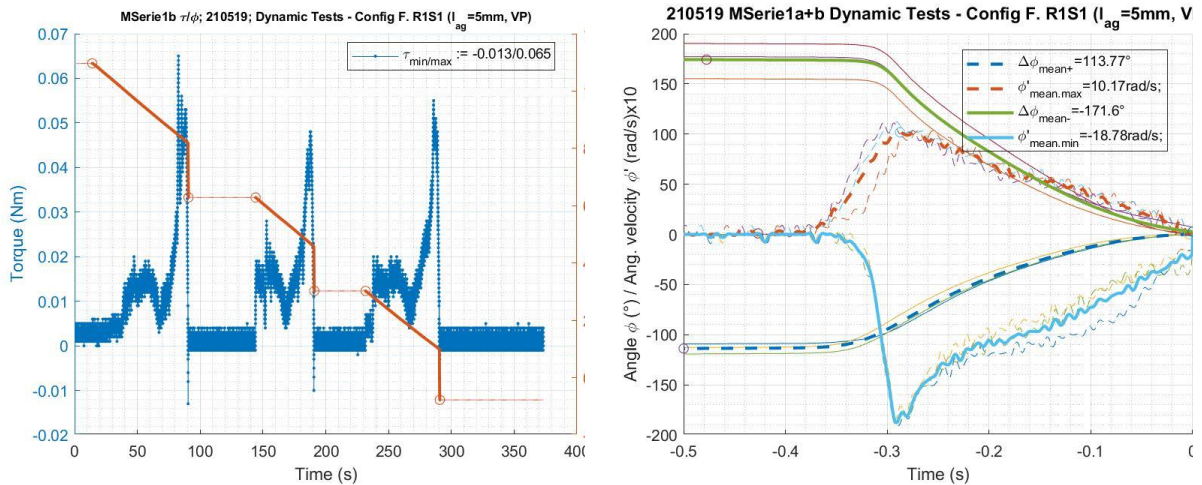

Fig. 18. Validation of an AIT signal– also compare config. 03.F in Fig. 10 and Fig. 11

Fig. 19 shows the same torque and motion signals as in chapter III (Fig. 13) and using the same parameter set – except having the EM torque spring's positive lobe 3x enlarged (compare also Fig. 6, rhs orange vs blue torque line). By carefully tuning the friction parameters (using model [17], main influence is shown parameter D_1 in diagrams), stiffness parameter $C_{r.amp} \cong 0.06$ for amplifying normalized torque signal of Fig. 6, rhs and a positive lobe amplification factor $C_{r.lobe +} \cong 3$ to realistic values (compare to Fig. 16, rhs and Fig. 6, rhs), the measured signals can be matched well in the limited interval, where the EM spring is active ($\gamma_{MS} \cong 103°$). Friction parameters are notoriously difficult to model and estimate. The used friction model [17] has been successfully applied for KEH harvester validations [18] and therefore no analytical friction model using the measured friction (Fig. 16) has been realized.
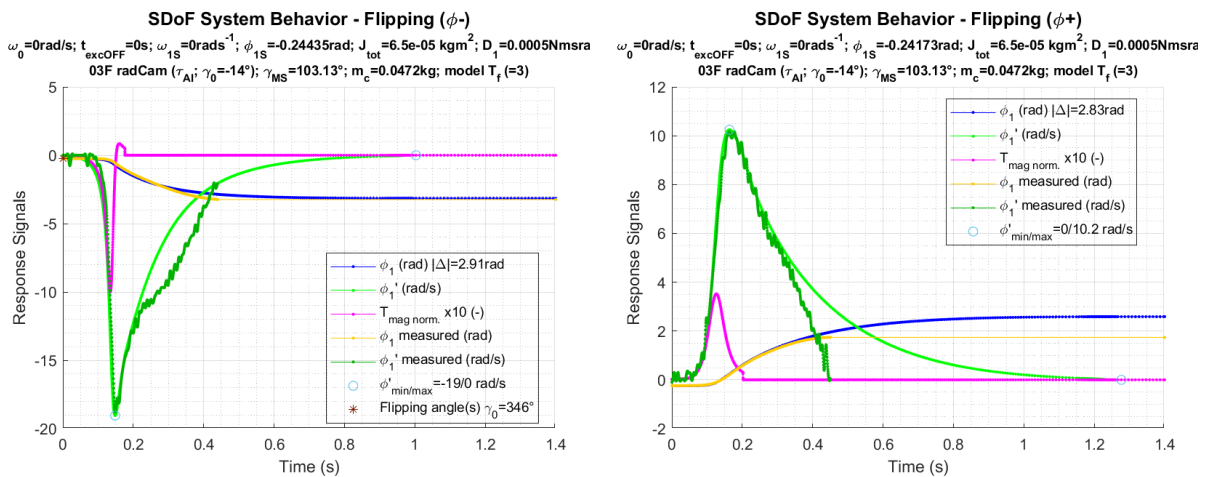

Fig. 19. Validation of an AIT signal in config. 03.F (setup shown in Fig. 10, rhs)

4.5 Discussion of Validation Measurements

With static tests the shapes of nonlinear EM-springs have been determined (Fig. 16) using a dynamic torque sensor (with integrated encoder). For measuring the commensurability of the spring, dynamic tests were exercised, using the torque sensor again (as absolute encoder). These experiments show, that for reference tests, the angular velocities are in both cw and ccw direction approximately the same (Fig. 17), but evidently different in the AIT spring system (Fig. 18). With regard to the presented configuration of 03.F, an AIT signal of approximately 10% could be found (compare Fig. 6, rhs, Fig. 11, bottom, Fig. 16, rhs), resulting in an estimated significant energy difference of $1.1mJ$. However, static tests are not conclusive to claim energy excess, as in the presented radial cam configuration (03.F), a noisy torque

signal is generated (Fig. 16, rhs). Yet, dynamic tests by letting flip the rotor PM out of the instable position show asymmetric motion signals (compare symmetric, Fig. 17 and asymmetric case, Fig. 18). Applying (II.15) on the lumped parameter model (Fig. 5), measuring and carefully estimating system parameters, validation (Fig. 19) has been done. Flipping in ccw, the max. ang. velocity is $-19\ rad/s$ vs. $+10.2\ rad/s$ in cw direction. The path signal also shows an imparity ($2.91 rad$ in ccw vs $2.83 rad$ in cw dir. for simulation and a measured difference of ca. 1rad, compare chapter 4.4, Fig. 18), but due to non-uniform friction (Fig. 15), this signal validation lacks accuracy.

V.   Conclusions

5.1   *Concluding Remarks of Simulations and Measurements*

Chapter I presents a systematic outline of resonant and nonresonant MEH systems, using also phenomenological approaches to investigate scientifically the topic of direct magnetic energy harvesting, contradicting in isolated cases the current knowledge described in excellent textbooks [14, 21, 22]. In chapter II, the important inequality of work done by magnetic forces (II.3) is shown and one method for torque calculation applying classical physics is presented as well as other well-known methods for modeling magnetic fields [4] is exercised. A lumped parameter model for testing torque signal is introduced. Chapter III presents an excerpt of a systematic investigation using geometrical current loop configurations. Each configuration test has been started with most simple current ring structures, such as only one current ring on rotor and stator and test it for energy excess. When such simulations confirmed unusual torque and energy behavior, additional current rings had been placed to create an approximately realistic PM structure, before testing it through experiments on a testbed. The used radial cam has a rather unusual kinematic – especially as the center of the revolving shaft becomes occupied. It is possible to conceive plenty of different and much simpler radial cam movements (see also Fig. 1). In some of the presented simulated PM structures, energy excess could be found (Fig. 7, rhs; Fig. 9 and Fig. 11).

Following the validation process of chapter IV, it is shown by measurements that an unequal amount of energy can be stored and released from the proposed EM spring system. Therefore, it is expected that the measured energy-surplus can be multiplied in a stiff rotor system, and a seemingly perpetual motion should be possible to achieve. Hence, carefully following the validation process, the question in the title of this article can be answered with yes. As required by the scientific method, the presented experiments need to be verified by other independent research groups. The underlying principle of regarding EM springs as mechanical springs [9, 11, 18] and using a rotary system and simple jumps out of the instable position in clockwise and counter-clockwise direction is very well suited and inexpensive. Energy excess with a radial cam could be then demonstrated. For linear systems, such energy surplus with large square PMs has already been shown [23] – this result has been verified by the author with analytical methods shown in chapter II, III, but not presented in this manuscript.

5.2   *General Concluding Remarks*

The energy source cannot yet be determined. However, the developed atomic model (published already close to 20a ago) from R. Mills [24–33] could be a very good candidate to help explain this phenomena (by modeling also iron, cobalt, nickel, neodymium atomic crystal structures with such presented methods). Two current working hypotheses can be conjectured: (1) we might deal here with a very slow nonradioactive decay process of PM structures, which might be slightly accelerated when using them in MEH systems or/and (2) free metal electrons (or electron pairs) might drop into a lower orbit (following Mills, it might be hydrino-like states of metals) and emit EM radiation which can be observed as an asymmetric torque signal in the macrocosm. Both needs to be tested – however, from an engineering point of view, the next step is to create with shown measurements a seemingly perpetual motion.

This research has been founded privately and with almost no funds. It is a mystery to me, why such important research, for which I asked for years when I was still a doctoral candidate, has not yet been done publicly. Political correctness cannot be an issue in science, as everything should be scrutinized with respect, rigor, and responsibility. We hit here (seemingly?) untouched research ground. It is hoped that this publication will change it. The author is happy to share even more details on presented work to any private or public research groups, who will use it for the advancement of human society.

Appendix A. Approximated radial cam

Approximated radial cam following [15] gives

$$r_{CAM}(\theta) \approx l_{PM}^* + l_e \left(1 - \frac{l_e}{2\, l_0} (\cos \theta)^2 + \sin \theta \right) \tag{V.1}$$

Parameter l_{PM}^* needs to be changed by an offset $l_{PM}^* = l_{PM} + l_e$. This function has an error of better than <1% for fraction $\frac{l_e}{l_0} < 0.25$– for this application error reaches 2%.
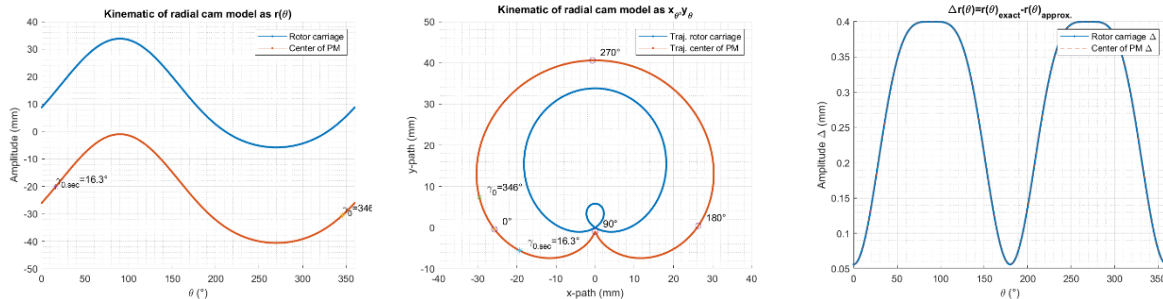

Fig. 20. Kinematic of PM and rotor carriage (both trajectories through the center of gravity) and numerical path error Δ using model DE (V.2) and (II.15)

Fig. 20, lhr, shows radius of θ $(= \phi)$; Fig. 20, middle, depicts developing x, y trajectory. For diagram orientation also angles 0°, 90°, 180° and 270° are shown and in addition, the main flipping point γ_0 as well as a secondary flipping point $\gamma_{0.sec}$ is shown. Note that system flips at γ_0, where the difference of max. and min. torque is found. On the rhs of Fig. 20, error of exact (V.2) and approximated (II.15) DE is shown.

Appendix B. Dynamics of exact and approximated radial cam

Fig. 21 depicts the calculated ang. path ϕ (blue) and its ang. velocity ϕ' (green) using the exact radial cam shown in eq. (II.5) and the approximated radial cam using (V.1) inserted in the general solution of numerical solution of eq. (II.14) . using Mathematica by setting parameters $D(\phi') = 0$, $C(\phi) = 0$ and $J_{tot} = 0$. Exemplarily, also a symmetric PM spring is shown (but not applied) to test flipping position, given here at $\gamma_0 = 346°$.
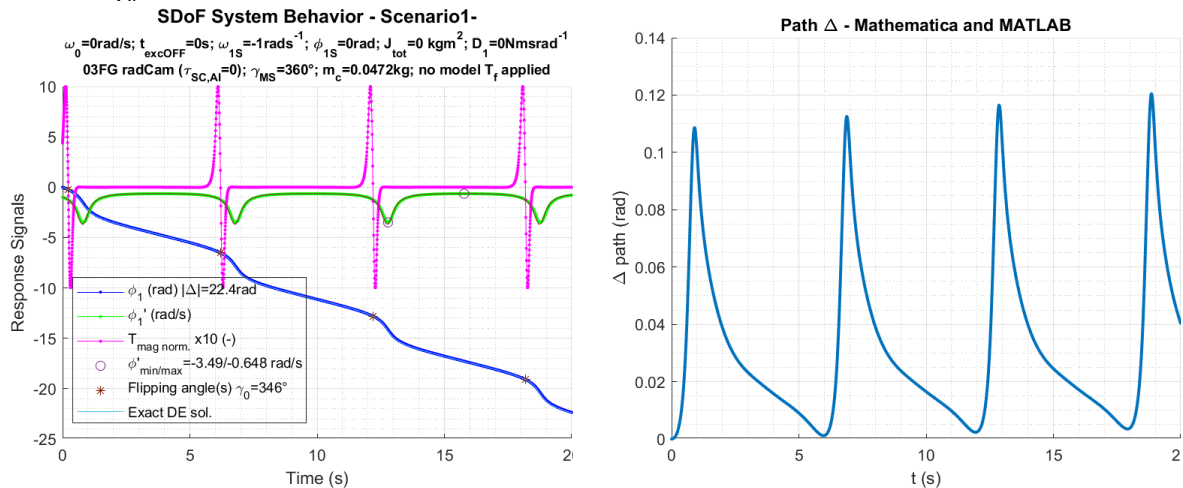

Fig. 21. Comparison of resulting trajectories no damping and no stiffness applied. Initial conditions: $\phi(0) = 0$ and , $\phi'(0) = -1 rad/s$ (lhr); path error of exact and approx. solution (rhs)

Parameters set to $m = 47.2g, l_e = 19.8mm, l_0 = 40mm, l_{PM} = -26mm$ (same parameters as in chapter 3.5). Set parameters and shown flipping points represent testbed flipping point positions. Note that exact and approximate DE solution match well.

Inserting in (II.14) the exact radial cam (II.5) gives:

$$\begin{aligned}
&\left(l_e{}^2 (\cos\phi)^2 \left(1 + \frac{l_e \sin\phi}{l_0 \sqrt{1 - \frac{l_e{}^2}{l_0{}^2}(\cos\phi)^2}} \right)^2 + \left(l_{PM} + l_0 \sec\phi \sin\left(\arccos\left(\frac{l_e}{l_0}\cos\phi \right) + \phi \right) \right)^2 \right) m\,\phi'' \\
&\quad - \frac{1}{4\left(l_e{}^2 - l_0{}^2(\sec\phi)^2 \right)^2} l_0\, l_e \left(-4l_0{}^3 + 4\,l_0\,l_e{}^2 - 2\,l_0{}^2\,l_{PM} \sqrt{4 - \frac{2l_e{}^2}{l_0{}^2} - \frac{2\,l_e{}^2}{l_0{}^2}\cos 2\phi} \right. \\
&\quad + l_e{}^2\,l_{PM} \sqrt{4 - \frac{2l_e{}^2}{l_0{}^2} - \frac{2\,l_e{}^2}{l_0{}^2}\cos 2\phi} \\
&\quad \left. + l_e{}^2\,l_{PM}\cos 2\phi \sqrt{4 - \frac{2l_e{}^2}{l_0{}^2} - \frac{2\,l_e{}^2}{l_0{}^2}\cos 2\phi} \right)(\sec\phi)^3 \left(l_0 \sqrt{1 - \frac{2\,l_e{}^2}{l_0{}^2}(\cos\phi)^2} \right. \\
&\quad \left. + l_e\,\sin\phi \right) m\,\phi'^2 + D(\phi')\,\phi' + C(\phi)\phi = 0
\end{aligned}$$

$$(V.2)$$

This expression is bulky, and an acceptable error of ϕ_A and the exact ϕ solution is found (Fig. 20, rhs), also, in respect to the investigated motion, a flip from the instable point towards stillstand. Therefore, expression of (II.15) can safely be applied.

Appendix C. Verification of superposition principle
Verification of superposition principle is shown in Fig. 22. Whether posing one single current loop on stator and rotor, or five loops (carrying five times smaller current) each, the same forces and energies will result. For such setups, the superposition principle holds.
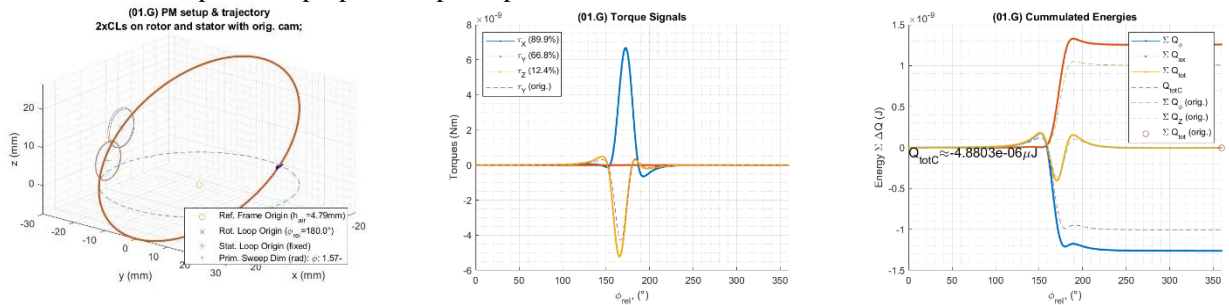

Fig. 22. Comparison of resulting forces using 1 current loop on stator and rotor as well as 5 current loops with each 5x smaller currents at the almost same position (shifted in x-direction by $10^{-12}m$ each)

Appendix D. Resonance frequency of torque sensor system
The resonance frequency ω_0 of the torque sensor system is given by:

$$\omega_0 = \sqrt{C_s \left(\frac{1}{J_1} + \frac{1}{J_2} \right)} \qquad (V.3)$$

where C_s is the stiffness of the sensor and $J_{1,2}$ are the cumulated inertias on measurement- and drive-side. For the Burster sensor 8661-5001, the spring stiffness is built as $C_s = 100\,\frac{rad}{s}$.

Appendix E. Simulation results using circular trajectories
In earlier validation attempts of AIT signals (system shown in chapter 3.2), following simulation using circular trajectories have been made. Like in chapter 3.5, also flipping from the instable rendez-vous point of stator and rotor PM is shown for circular trajectories using PM springs of type τ_{SC}, τ_{AC}, τ_{AI} (compare Fig. 1 C).
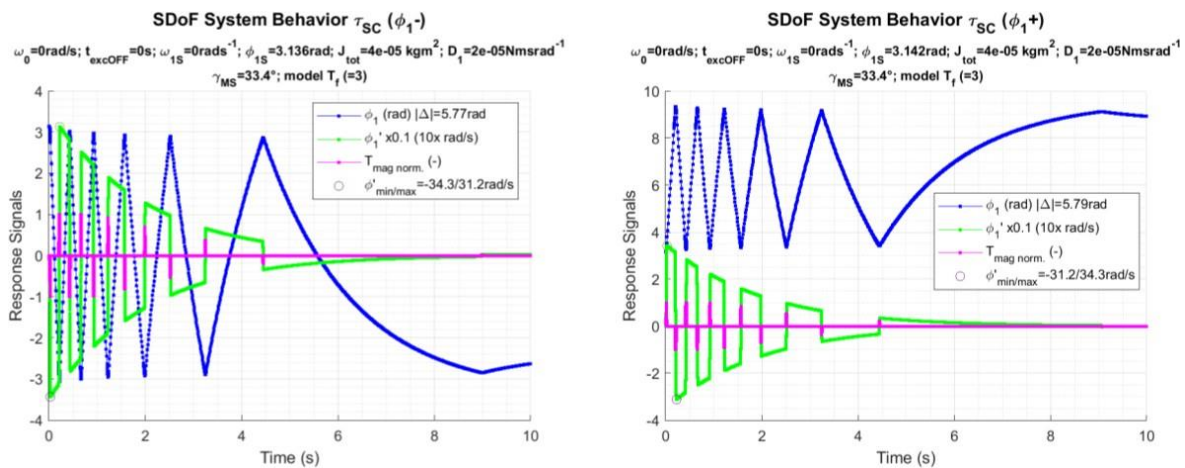
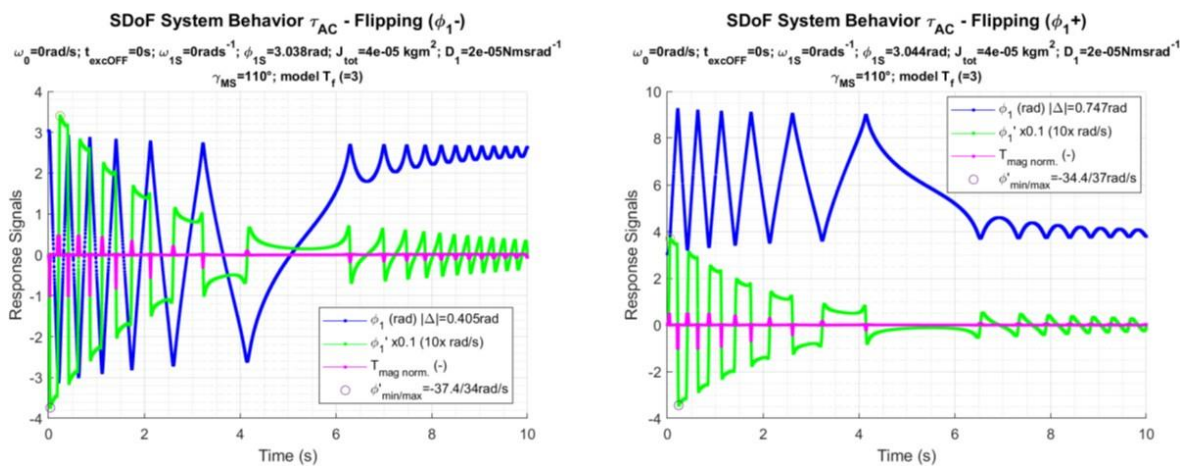**Fig. 23.** Nonlinear symmetric commensurable torque spring τ_{SC} behavior

Fig. 24. Nonlinear asymmetric commensurable torque spring τ_{AC} behavior
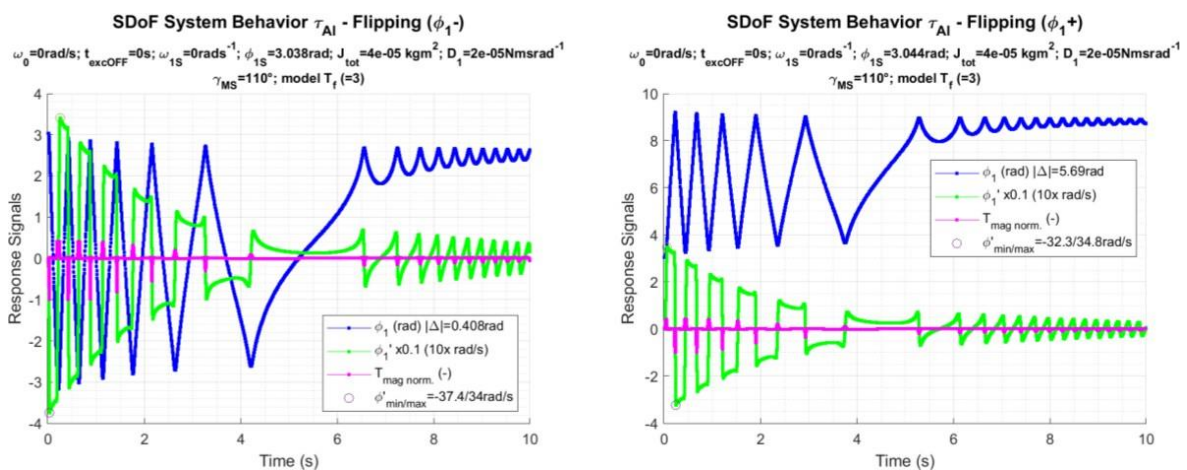

Fig. 25. Nonlinear asymmetric incommensurable torque spring τ_{AI} behavior

A negative (rhs) and positive (lhs) flipping of ϕ_1 with the initial condition $\phi_{1S+} = 3.142 rad$, $\phi_{1S-} = 3.136 rad$ (Fig. 23) and $\phi_{1S+} = 3.044 rad$, $\phi_{1S-} = 3.038 rad$ (Fig. 24 and Fig. 25) of the rotor is shown having such different torque springs applied. The same 3 signals are depicted in each figure: the motion signals ϕ_1 (path) and ϕ_1' (its ang. velocity signal) and the nonlinear normalized spring signal $T_{mag}(t)$. Markers, 'o' show the first max. and min. ang. velocity after starting a flip. Note that a negative flip will generate the same min. and max. ang. velocities, but just swapped. This simulation experiment manifests an energy surplus only when applying a τ_{AI} signal. Fig. 25 shows the maximum and minimum ang. velocities ϕ'_{max} and ϕ'_{min} of the simulated EM springs (τ_{SC}, τ_{AC} and τ_{AI}) when flipping

occurs towards a positive resp. negative ϕ given a nonlinear friction model. Only a different ang. velocity occurs when we deal with an asymmetric incommensurable torque spring τ_{AI}, as expected. The simulated max. and min. ang. velocities for this case is also given for linear (only viscous friction) and nonlinear friction [18]; the slight value differences between linear and nonlinear friction depend on the chosen parameter set.

Table 4
Max. ang. velocities at limit of angle of influence

Symbol	Value	Unit	Description
$\phi'_{\max(\tau_{SC})}$	+34.3	rad/s	End ang. vel. for a pos. flip
$\phi'_{\min(\tau_{SC})}$	−34.3	rad/s	End ang. vel. for a neg. flip
$\phi'_{\max(\tau_{AC})}$	+37.0	rad/s	End ang. vel. for a pos. flip
$\phi'_{\min(\tau_{AC})}$	−37.0	rad/s	End ang. vel. for a neg. flip
$\phi'_{\max(\tau_{AI})}$	+34.8	rad/s	End ang. vel. for a pos. flip
$\phi'_{\min(\tau_{AI})}$	−37.4	rad/s	End ang. vel. for a neg. flip
$\phi'_{\max(\tau_{AI})}$	+34.4	rad/s	End ang. vel. for a pos. flip (τ_D lin.)
$\phi'_{\min(\tau_{AI})}$	−37.2	rad/s	End ang. vel. for a neg. flip (τ_D lin.)

Appendix F. Additional path and torque data for dynamic validation
Additional torque and path signals are shown in Fig. 26. Diagram on the lhs shows the dynamic situation, revolving clockwise (compare Fig. 18, where only revolving ccw is shown). Fig. middle and lhs shows an additional measurement set of cw and ccw direction.
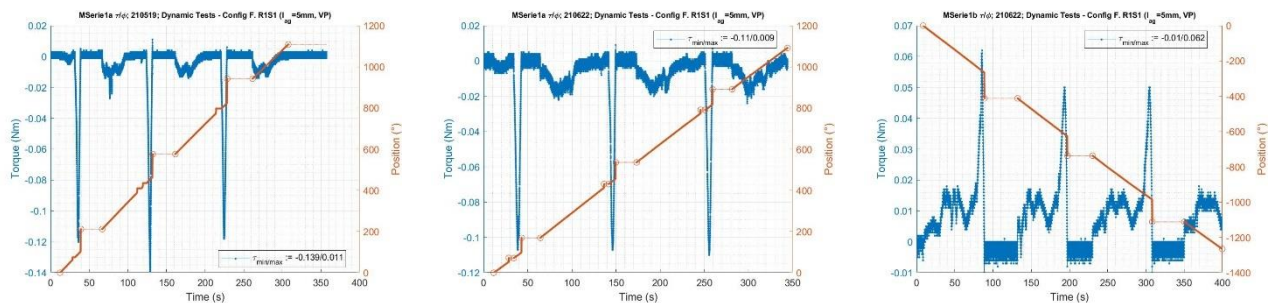

Fig. 26. Torque (blue) and path (red) data from measurements

It is interesting, that in cw direction, before reaching γ_0, pre-flips can be observed at 28.39s, 413.78s and 772.88s, creating jumps of 17.6°, 17.3° and 18.2°, (see middle fig.; also, on the lhs visible, but weaker). These pre-flips stem from the fact, that the calculated torque signal (Fig. 6) and the measured torque signal (Fig. 16) cross twice the zero-torque line (in Fig. 16 around 70° and 90°). Together with the noisy friction torque signal, they create such pre-jumps. Note also, that adding the path of these pre-flips to the main flip (middle figure, occurring at 43.01s, 149.80s and 259.50s), will make the path signal still asymmetric.

Appendix G. Validation attempt results using circular trajectories
Earlier attempts were made, using circular trajectories of configurations 10.A (Fig. 7, rhs). Using such circular trajectories are most simple to prototype and a calculated AIT signal of ca. 5% asymmetry can be achieved. Furthermore, by cumulating on a stiff rotor such torque asymmetries, an almost 100% asymmetric signal can be realized – theoretically. Measurements showed however, that such weak asymmetric signal addition will not cumulate in a larger measurable asymmetry using such geometrical dimensions. Dynamic measurements did not indicate a clear asymmetric ang. velocity signal (not shown in Fig. 27).
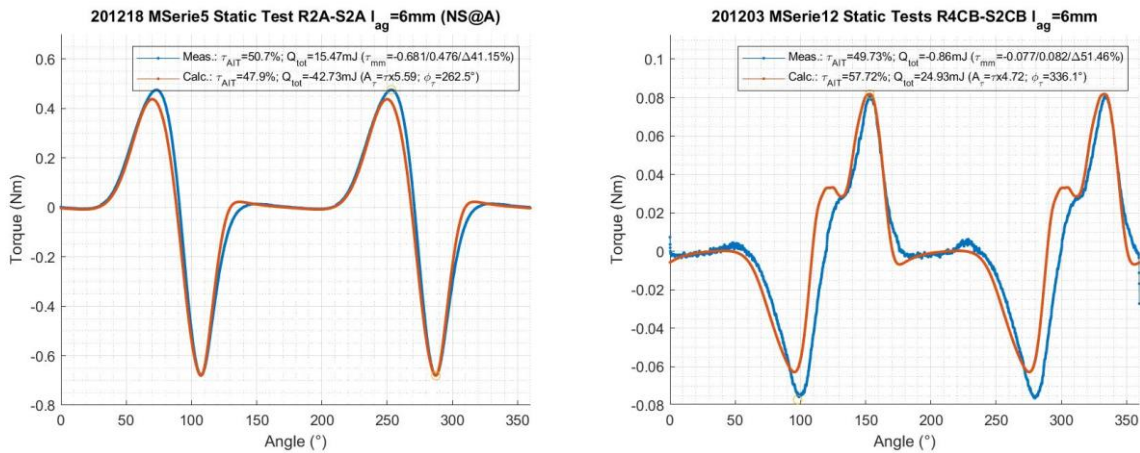
Fig. 27. Static validation tests with two (lhs) and four (rhs) symmetrically distributed rotor sets (by using configuration principle of 10.A)

References

[1] S. Babic and C. Akyel, "Magnetic Force Between Inclined Circular Filaments Placed in Any Desired Position," *IEEE Trans. Magn.*, vol. 48, no. 1, pp. 69–80, 2012, doi: 10.1109/TMAG.2011.2165077.

[2] S. I. Babic and C. Akyel, "Magnetic Force between Inclined Circular Loops (Lorentz Approach)," *PIER B*, vol. 38, pp. 333–349, 2012, doi: 10.2528/PIERB12011501.

[3] J. M. Camacho and V. Sosa, "Alternative method to calculate magnetic field of permanent magnets with azimuthal symmetry," *Revista Mexicana de Fisica*, 2013.

[4] D. Spreemann and Y. Manoli, *Electromagnetic Vibration Energy Harvesting Devices: Architectures, Design, Modeling and Optimization*. Dordrecht: Springer Netherlands, 2012.

[5] S. P. Beeby *et al.,* "A micro electromagnetic generator for vibration energy harvesting," *J. Micromech. Microeng.*, vol. 17, no. 7, pp. 1257–1265, 2007, doi: 10.1088/0960-1317/17/7/007.

[6] B. P. Mann and B. A. Owens, "Investigations of a nonlinear energy harvester with a bistable potential well," *Journal of Sound and Vibration*, vol. 329, no. 9, pp. 1215–1226, 2010, doi: 10.1016/j.jsv.2009.11.034.

[7] E. M. Yeatman, "Energy harvesting from motion using rotating and gyroscopic proof masses," *Proceedings of the Institution of Mechanical Engineers, Part C: Journal of Mechanical Engineering Science*, vol. 222, no. 1, pp. 27–36, 2008, doi: 10.1243/09544062JMES701.

[8] M. Yildiz, "Device having an arrangement of magnets," WO 2009/019001 A3 2009/019001 A3.

[9] L. Kurmann and Y. Jia, "Oscillators with Nonpolar Magnetic Repulsion System and its Use in Rotary Nonresonant and Resonant Kinetic Energy Harvesters," *IOSR Journal of Applied Physics*, vol. 10, no. 4, pp. 57–76, 2018, doi: 10.9790/4861-1004015778.

[10] J. L. Duarte, "Modeling the Yildiz Motor revisited," *Eindhoven University of Technology Research Report*, 2018, doi: 10.6100/6B67487A-BD78-4A24-BDD1-D7B9B3DBD5B7.

[11] L. Kurmann and J. L. Duarte, "Generation of asymmetric incommensurable torque signals," *J. Phys.: Conf. Ser.*, vol. 1407, p. 12066, 2019, doi: 10.1088/1742-6596/1407/1/012066.

[12] J. Duarte, "Essay on Magnetic Wind Mills Part I Analysis and Design: Research Report," Eindhoven University of Technology, 2019.

[13] S. J. Chapman, *Electric machinery fundamentals,* 4th ed. New York NY: McGraw-Hill Higher Education, 2005.

[14] D. J. Griffiths, *Introduction to electrodynamics,* 3rd ed. Upper Saddler River, N.J.: Prentice Hall; London : Prentice-Hall International, 1999.

[15] K. Groth and G. Rinne, *Verbrennungskraftmaschinen*. Braunschweig: Vieweg, 1994.

[16] L. H. de Medeiros, G. Reyne, and G. Meunier, "About the distribution of forces in permanent magnets," *IEEE Trans. Magn.*, vol. 35, no. 3, pp. 1215–1218, 1999, doi: 10.1109/20.767168.

[17] M. Charu, D. Warren, S. Wallace, and H. Guoqiang, *A New Continuously Differentiable Friction Model for Control Systems Design*. Piscataway N.J.: IEEE, 2005.

[18] L. C. Kurmann, "Rotary nonresonant energy harvesting," Dissertation, IMTEK, University of Freiburg, Breisgau, Germany, 2020.000Z. Accessed: 6/26/2020. [Online]. Available: https://freidok.uni-freiburg.de/data/151794

[19] J.-P. Yonnet, "Permanent magnet bearings and couplings," *IEEE Trans. Magn.*, vol. 17, no. 1, pp. 1169–1173, 1981, doi: 10.1109/TMAG.1981.1061166.

[20] L. Kurmann and P. Grubert, "Modelling of Asymmetric Incommensurable Torque Signals," [Online]. Available: https://www.comsol.com/conference2018/view-paper-file/92091

[21] H. Klingbeil, *Elektromagnetische Feldtheorie für Fortgeschrittene*. Berlin, Heidelberg: Springer Berlin Heidelberg, 2018.

[22] D. J. Griffiths, *Introduction to quantum mechanics*. Englewood Cliffs: Prentice Hall; London : Prentice-Hall International, 1995.

[23] K. Kozeka, "A Motor Driven by Permanent Magnets Alone; A Clean and Abundant Source of Electromagnetic Energy from Iron and Other Ferromagnetic Materials," *NS*, vol. 09, no. 09, pp. 319–329, 2017, doi: 10.4236/ns.2017.99031.

[24] R. L. Mills, *The grand unified theory of classical quantum mechanics - Volume I,* 2018th ed. Cranbury, NJ: Blacklight Power, 2001.

[25] R. L. Mills, *The grand unified theory of classical quantum mechanics - Volume II,* 2001st ed. Cranbury, NJ: Blacklight Power, 2001.

[26] R. L. Mills, *The grand unified theory of classical quantum mechanics - Volume III,* 2001st ed. Cranbury, NJ: Blacklight Power, 2001.

[27] R. L. Mills, "The Nature of the Chemical Bond Revisited and an Alternative Maxwellian Approach," *Physics Essays*, vol. 17,

no. 3, pp. 342–389, 2004, doi: 10.4006/1.3025699.

[28] R. L. Mills, "Exact Classical Quantum-Mechanical Solutions for One- through Twenty-Electron Atoms," *Physics Essays*, vol. 18, no. 3, pp. 321–361, 2005, doi: 10.4006/1.3025747.

[29] R. L. Mills, "Exact Classical Quantum-Mechanical Solutions for One- through Twenty-Electron Atoms," *Physics Essays*, vol. 18, no. 3, pp. 321–361, 2005, doi: 10.4006/1.3025747.

[30] R. L. Mills, "The fallacy of Feynman's and related arguments on the stability of the hydrogen atom according to quantum mechanics," vol. 2, 2005.

[31] R. L. Mills, "Maxwell's Equations and QED: Which Is Fact and Which Is Fiction?," *Physics Essays*, vol. 19, no. 2, pp. 225–262, 2006, doi: 10.4006/1.3025792.

[32] R. L. Mills, "Physical Solutions of the Nature of the Atom, the Photon, and Their Interactions to Form Excited and Predicted Hydrino States," *Physics Essays*, vol. 20, no. 3, pp. 403–460, 2007, doi: 10.4006/1.3153414.

[33] R. L. Mills, "Exact classical quantum mechanical solution for atomic helium which predicts conjugate parameters from a unique solution for the first time," *Physics Essays*, vol. 21, no. 2, pp. 103–141, 2008, doi: 10.4006/1.3009282.